nature communications

Article

https://doi.org/10.1038/s41467-025-58336-x

Optogenetic activation of mechanical nociceptions to enhance implant osseointegration

Received: 22 September 2024

Accepted: 18 March 2025

Qijin Wang[1,2,3,7], Yang Chen[1,2,3,7], Haiqi Ding[1,2,3,7], Yuanqing Cai[1,2,3,7], Xuhui Yuan[1,2,3], Jianhua Lv[1,2,3], Jiagu Huang[1,2,3], Jiexin Huang[1,2,3], Chaofan Zhang[1,2,3], Zihao Hong[1,2,3], Hongyan Li[1,2,3], Ying Huang[1,2,3], Jiamin Lin[1,2,3], Lin Yuan[1,2,3], Lan Lin[1,2,3], Shaolin Yu[1,2,3], Canhong Zhang[1,2,3], Jianhua Lin[1,2,3], Wenbo Li[1,2,3], Cheng Chang[4], Bin Yang[5,6] ✉, Wenming Zhang[1,2,3] ✉ & Xinyu Fang[1,2,3] ✉

Orthopedic implants with high elastic modulus often suffer from poor osseointegration due to stress shielding, a phenomenon that suppresses the expression of intracellular mechanotransduction molecules (IMM) such as focal adhesion kinase (FAK). We find that reduced FAK expression under stress shielding is also mediated by decreased calcitonin gene-related peptide (CGRP) released from Piezo2$^+$ mechanosensitive nerves surrounding the implant. To activate these nerves minimally invasively, we develop a fully implantable, wirelessly rechargeable optogenetic device. In mice engineered to express light-sensitive channels in Piezo2$^+$ neurons, targeted stimulation of the L2-3 dorsal root ganglia (DRG) enhances localized CGRP release near the implant. This CGRP elevation activates the Protein Kinase A (PKA)/FAK signaling pathway in bone marrow mesenchymal stem cells (BMSCs), thereby enhancing osteogenesis and improving osseointegration. Here we show that bioelectronic modulation of mechanosensitive nerves offers a strategy to address implant failure, bridging neuroregulation and bone bioengineering.

Orthopedic implants are commonly used for the replacement of weight-bearing bones, such as in artificial joints, spinal fusion, and bone fixation or filling[1]. Even though implants typically yield favorable outcomes, around 10% of them end up failing[2]. Notably, over half of these unsuccessful cases stem from aseptic loosening triggered by the subpar osseointegration of implants[3,4]. Metals commonly used for orthopedic implants, such as titanium alloys and cobalt-chromium-molybdenum alloys, possess good mechanical properties and corrosion resistance[5,6]. However, their elastic modulus is significantly higher than that of human cortical bone. This mismatch can result in insufficient stress stimulation of the surrounding bone tissue, leading to the phenomenon known as stress shielding[7]. This leads to localized bone resorption, implant loosening, ultimately compromising long-term stability[6,8]. The loosening of implants significantly exacerbates the

---

[1]Department of Orthopaedic Surgery, National Regional Medical Center, Binhai Campus of the First Affiliated Hospital, Fujian Medical University, Fuzhou, China. [2]Department of Orthopedic Surgery, The First Affiliated Hospital of Fujian Medical University, Fuzhou, China. [3]Fujian Provincial Institute of Orthopedics, the First Affiliated Hospital, Fujian Medical University, Fuzhou, China. [4]Institute of New Materials, Guangdong Academy of Sciences, Guangdong-Hong Kong Joint Laboratory of Modern Surface Engineering Technology, Guangdong Provincial Key Laboratory of Modern Surface Engineering Technology, Guangzhou, Guangdong, PR China. [5]Department of Laboratory Medicine, The First Affiliated Hospital of Fujian Medical University, Fuzhou, China. [6]Department of Laboratory Medicine, National Regional Medical Center, Binhai Campus of the First Affiliated Hospital, Fujian Medical University, Fuzhou, China. [7]These authors contributed equally: Qijin Wang, Yang Chen, Haiqi Ding, Yuanqing Cai. ✉e-mail: yangbin2864@163.com; zhangwm0591@fjmu.edu.cn; fangxinyu0417@fjmu.edu.cn

medical burden and socioeconomic costs associated with revision procedures[9].

To enhance implant osseointegration, Ti6Al4V micro-lattice materials and Polyether Ether Ketone (PEEK) materials are utilized in orthopedic implants due to their tunable elastic modulus[10,11]. However, in weight-bearing regions of the limbs, these materials are prone to deformation and breakage due to insufficient mechanical strength[12]. Consequently, methods are developed to enhance osseointegration through surface modification of implants; however, poor osseointegration cannot be entirely circumvented[13]. Regardless of the modifications made to the implant, a persistent issue arises in clinical settings: once stress shielding occurs and loosening ensues following the implantation of prostheses, there are currently no remedial measures available other than additional surgical intervention.

Mechanical stress influences the remodeling of intracellular stress fibers and the activity of intracellular mechanotransduction molecules (IMM) such as integrins, Focal Adhesion Kinase (FAK), Microtubule-Actin Crosslinking Factor 1 (MACF1), and Extracellular Signal-Regulated Kinase (ERK)[14,15], thereby regulating the migration, proliferation, and differentiation of bone-related cells. The decrease in the expression of IMM signaling molecules resulting from stress shielding is a significant factor that hinders the osseointegration of implants. Therefore, exploring effective strategies to modulate the activity of IMM signaling molecules in bone-related cells within this unalterable stress environment surrounding previously implanted devices presents a bypass approach to alleviate the adverse effects of stress shielding on osseointegration.

Bone tissue is innervated by a dense network of sensory nerves, with the most commonly distributed sensory nerves being calcitonin gene-related peptide (CGRP)-positive nociceptors[16]. Nociceptors can sense stimuli such as mechanical pressure, cold, and heat[17]. Upon receiving these stimuli, the terminal fibers of these nerves release CGRP, which can participate in the regulation of bone metabolism and integration processes. For example, CGRP promotes the proliferation of bone marrow mesenchymal stem cells (BMSCs) and the differentiation of osteoblasts, thereby affecting bone mass and tendon-bone healing[18]. CGRP$^+$ piezo2$^+$ fibers, which sense mechanical stress, account for approximately 40% of nociceptors innervating bones[19]. Additionally, CGRP regulates the expression of IMM[20]. Therefore, the regulatory role of Piezo2$^+$ nociceptors in bones may have potential in addressing the inhibition of osseointegration caused by insufficient mechanical stress, although the mechanisms and interventions require further exploration.

As a peptide lacking a quaternary protein structure, CGRP is rapidly degraded in plasma, which limits the application of exogenous CGRP in bone healing[21]. Endogenous CGRP is synthesized in the dorsal root ganglia (DRG), with its transcription being highly regulated by depolarization[22]. Electrical stimulation (ES) of the DRG can promote nociceptor depolarization and CGRP secretion to aid in the healing of osteoporotic fractures[21]. However, non-targeted stimulation may cause discomfort and other side effects. Achieving highly selective stimulation of nociceptors related to mechanical stress around implants remains challenging. Optogenetics integrates multidisciplinary knowledge from optics, software control, and genetic manipulation to target and manipulate specific neuronal subpopulations, such as excitatory and inhibitory neurons[23]. Currently, a fully implantable, flexible, and wirelessly rechargeable optogenetic stimulation (OS) device suitable for rats[24]. However, its size and weight exceed the load capacity for many transgenic mice used in neuroscience research.

In this work, we present the smallest, lightest fully implantable, wirelessly rechargeable OS device to date. Using mice expressing the light-sensitive protein Channelrhodopsin-2 (ChR2)[25], we achieve controllable stimulation of the DRG in freely moving, awake mice. This method stimulates Piezo2$^+$ nociceptors and induces CGRP release, reversing the suppression of the IMM FAK expression caused by insufficient mechanical stress, thereby promoting the osseointegration of tibial implants with bone in mice. This demonstrates that the wirelessly rechargeable OS device, combined with nociceptor regulation, has broad applications and potential in promoting implant osseointegration in clinical applications and in neuro-bone regulation research. Beyond conventional improvements in metallic materials or surface modifications, the primary advantage of our research resides in providing a solution for patients with pre-existing implants that have demonstrated inadequate osseointegration.

Results

Delayed osseointegration due to stress shielding is associated with diminished expression of mechanotransduction molecules

To optimize the simulation of the biomechanical environment associated with total joint arthroplasty, we selected a mouse knee joint implantation model based on previous literature reports[26]. To investigate the impact of stress factors induced by different elastic moduli implants on implant osseointegration, we designed and 3D printed two types of implants: (i) solid Ti6Al4V knee implants with a high elastic modulus (114 Gpa) (Fig. 1a I), and (ii) Ti6Al4V implants with a 25% overall porosity, with an elastic modulus (28 Gpa) closer to that of bone (Fig. 1a II). The two types of implants were implanted into the tibial plateau of the right knees of mice (Supplementary Fig. 1a). Two weeks after implantation, tibial specimens from the Ti6Al4V and Ti6Al4V (Internal porosity) groups were collected and subjected to hard tissue sectioning followed by methylene blue-acid fuchsin staining (Fig. 1b). The results showed that, despite the hydrophilicity of the two materials being similar (Supplementary Fig. 1b), bone-implant contact percentage (BIC%) around the Ti6Al4V implants was significantly less than that around the Ti6Al4V (Internal porosity) implants (Fig. 1c). This indicates that mechanical factors influence the osseointegration capacity of implants to a certain extent.

One week after model establishment, transcriptomic sequencing analysis of bone tissue surrounding the implants in both groups was performed. The heatmap of differential gene expression (Fig. 1d) revealed significant differences in mRNA expression patterns between the Ti6Al4V and Ti6Al4V (Internal porosity) groups, indicating altered gene expression in the tissue surrounding the Ti6Al4V (Internal porosity) implants. Notably, genes such as ptk2 (encoding FAK), Piezo2, and Ogn were significantly upregulated. These genes are closely associated with mechanotransduction, cell differentiation, migration, and proliferation.

To further explore the activated biological functions and signaling pathways, we conducted Gene Ontology (GO) enrichment analysis and KEGG pathway analysis. GO enrichment analysis results (Fig. 1e) showed that the upregulated pathways in the Ti6Al4V (Internal porosity) group were mainly involved in response to stimulus, ossification, osteoblast differentiation, and extracellular matrix (ECM) organization. These processes are crucial for the development, structural maintenance, and functional realization of the skeletal system. KEGG enrichment analysis (Fig. 1f) revealed that the upregulated pathways in the Ti6Al4V (Internal porosity) group included the focal adhesion pathway, TGF-beta signaling pathway, PI3K-Akt signaling pathway, and ECM-receptor interaction. These are key components of cell signal transduction, cell adhesion, and interactions between the ECM and cell receptors, all of which are essential for bone formation and skeletal system development. Within the focal adhesion pathway, the key protein FAK acts as an important signaling molecule mediating interactions between the extracellular matrix and the intracellular cytoskeleton under mechanical stress[27]. Similarly, GSEA analysis (Fig. 1g) demonstrated that the bone mineralization capability in the Ti6Al4V (Internal porosity) group was enhanced compared to the Ti6Al4V group.

We further validated the changes in FAK and key osteogenic genes from 0 to 21 days post-implantation. It was found that the expression of

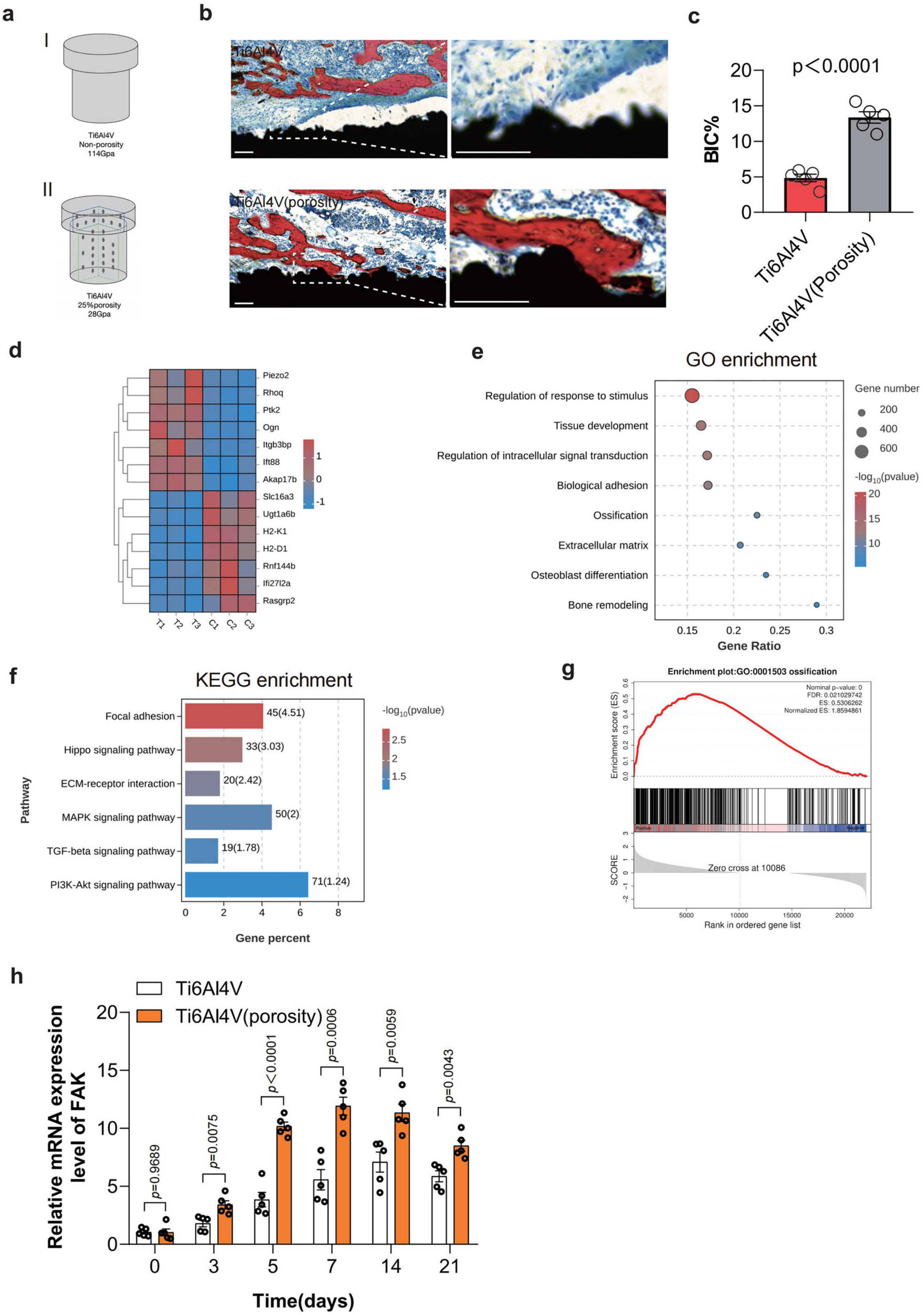

Fig. 1 | Stress shielding-induced delay in osseointegration is associated with low expression of mechanical signaling molecules. **a** Schematic diagram of mouse tibial implants with Ti6Al4V knee implants (114Gpa) and Ti6Al4V implants with a 25% overall porosity (28Gpa). **b**, **c** Methylene blue-acid fuchsin staining and quantitative analysis of bone tissue sections containing implants at two weeks. Scale bars: 10×: 100µm, 40×: 100µm. Data are presented as mean ± SEM (*n* = 5 biologically independent experiments). *P*-values were calculated using Two-tailed Student's *t* tests. **d** Transcriptomic heatmap of peri-implant bone tissue at one week. **e** Transcriptomic GO enrichment analysis plot of peri-implant bone tissue at one week. **f** Transcriptomic KEGG enrichment analysis plot of peri-implant bone tissue at one week. **g** Transcriptomic GSEA plot of peri-implant bone tissue at one week. **h** The expression of FAK at mRNA levels in peri-implant bone tissue from 0 to 21 days. Data are presented as mean ± SEM (*n* = 5 biologically independent experiments). *P*-values were calculated using Two-tailed Student's *t* tests. (BIC%: bone-implant contact percentage, FAK: focal adhesion kinase. **h** compared to the expression of FAK at mRNA levels of Ti6Al4V group at day 0). Source data are provided as a Source Data file.

FAK in the Ti6Al4V group was consistently lower than that in the Ti6Al4V (Internal porosity) group at all time points (Fig. 1h). Moreover, the peak expression in the Ti6Al4V group (14 days versus 7 days) was significantly delayed compared to the Ti6Al4V (Internal porosity) group (Fig. 1h). Additionally, the expression of key osteogenesis-related genes regulated by FAK[28], such as alkaline phosphatase (ALP), ecombinant Runt- related transcription factor 2 (RUNX2), osteopontin (OPN), and osteocalcin (OCN), was also inhibited (Supplementary Fig. 1c–f).

High elastic modulus implants decrease CGRP release of Piezo2$^+$ nociceptors, inhibiting FAK expression and implant osseointegration

The expression of the intracellular mechanosensitive protein FAK in implants with varying elastic moduli may be influenced not only by the mechanical forces experienced by the cells but also by sensory neurotransmitters such as CGRP[20]. Subclasses of nociceptive neurons, specifically piezo2$^+$ pressure-sensitive neurons, are capable of sensing changes in pressure within the bone marrow[29]. We began by injecting the retrograde tracer Fast Blue (FB) into the bone marrow cavity of C57BL/6 mice following tibial medullary expansion (Fig. 2a), and performed simultaneous immunofluorescence staining for piezo2 and CGRP in the DRG 3 days later. The stress-sensitive neurons associated with the upper portion of the tibia and its vicinity are derived from branches of the sciatic nerve, with their corresponding upper-level neurons primarily located in the L2-3 DRGs[30]. Within the FB-labeled L2-3 DRGs, a majority were CGRP$^+$ (Fig. 2b), among which ~ 36% were piezo2$^+$ (Fig. 2c), indicating a wide distribution of pressure-sensitive neurons at the bone interface in contact with tibial implants. We then utilized the piezo2 activation indicator FM1-43FX to determine whether mechanosensitive neurons were activated after implantation[31]. FM1-43FX was administered intraperitoneally to both the implant groups (Ti6Al4V (Internal porosity) and Ti6Al4V) and a sham surgery group. Immunofluorescent staining of L2-3 DRGs performed 24 hours after FM1-43FX injection revealed a significantly higher number of positive DRGs in the implant groups compared to the sham group, with the Ti6Al4V group exhibiting notably fewer activated DRGs than the Ti6Al4V (Internal porosity) group (Fig. 2d-e). Given that piezo2$^+$ DRGs are predominantly CGRP$^+$, we assessed the levels of CGRP expression at the same time point using ELISA. The results showed that the expression of CGRP in the bone tissue surrounding the implants was significantly reduced in the Ti6Al4V group compared to the Ti6Al4V (Internal porosity) group (Fig. 2f). Another subclass of nociceptive neurons within the bone, the TRPV1$^+$ thermosensitive neurons, are also widely distributed, Simultaneously, Piezo1 and Piezo2 are recognized as important mechanosensitive receptors. To detect the role of TRPV1$^+$, Piezo1$^+$ and Piezo2$^+$ in the CGRP release affected by changes in the elastic modulus, we generated TRPV1-DTR, Piezo1-DTA and Piezo2-DTR animals (Supplementary Figs. 2a, 2c and 2e) to ablate the TRPV1, Piezo1 and Piezo2-positive neurons. And evaluated the effect of Ti6Al4V and Ti6Al4V (Internal porosity) implants on CGRP expression. In animals with TRPV1$^+$ and Piezo1$^+$neuron ablation, the enhancing effect of Ti6Al4V (Internal porosity) implants on CGRP release remained (Supplementary Fig. 2b, d), whereas deletion of Piezo2$^+$ neurons reduction the expression of CGRP in both groups (Supplementary Fig. 2f), suggesting that Piezo2$^+$ neurons are the predominant nociceptor subclass that responds to pressure-associated CGRP release.

We further assessed whether the differences in nerve activation states caused by implants with varying elastic moduli affect the expression of the pressure-sensitive gene FAK in the bone tissue surrounding the implant. Direct injections of CGRP were administered around the Ti6Al4V group implants immediately after implantation. Observations from micro-CT results two weeks later (Fig. 2g) revealed that the Ti6Al4V+Inject CGRP group exhibited significantly higher bone volume/total volume (BV/TV), trabecular thickness (Tb.Th), number of trabeculae (Tb.N), bone mineral density of bone volume (BMD of BV), and bone-implant contact percentage (BIC%), while having a significantly lower trabecular separation (Tb.Sp) compared to the Ti6Al4V group, approaching values similar to those of the Ti6Al4V (Internal porosity) group (Fig. 2h). Moreover, the injection of CGRP enhanced the expression of FAK (Supplementary Fig. 2g). This suggests that the reduced activation of mechanosensitive neurons and the suppression of CGRP expression caused by implants with a high elastic modulus may be related to the delayed peak of FAK expression.

Design of a Wireless, Rechargeable, Fully Implantable OS Device for Stimulation of Mouse DRG

To perform complex OS manipulations of the DRG in mice with minimal impact on their normal behavior, we integrated the latest advancements in materials science, electrical engineering, and neuroscience to design an advanced system. This system enables accurate and repeatable OS of the DRG while the mice are freely active, independent of their position and movement. Figure 3a illustrates a schematic breakdown of the wireless charging and smartphone-controlled OS components, which consist of four main functional elements: (I) a rechargeable lithium battery (10 mAh, 0.15 g); (II) a Bluetooth Low Energy (BLE) system-on-chip (SoC) for wireless control of the system; (III) a power management circuit equipped with an electromagnetic induction coil and coil antenna, primarily responsible for harvesting radio frequency (RF) energy and converting it into direct current (DC) charging current for the battery; and (IV) two efficient μ-LEDs flexible arrays that can be anchored around the DRGs. These μ-LEDs are embedded in ultrasoft polymer cushions (33.4 kPa, 1400 μm thick) that directly surround the DRG, ensuring precise OS. The functional components are encapsulated in biocompatible packaging made of polydimethylsiloxane (PDMS; 600 μm thick) and Parylene C (7 μm thick, 0.083 g mm m−2 day−1 water vapor permeability). This soft polymer encapsulation, not only provides protection against biological fluids and external impacts but also ensures the adaptability and reliable operation of the device in vivo[24]. The OS device is placed on the dorsal side of the mouse. Prior to the experiment, the device is implanted near the DRGs and anchored at both ends of the μ-LEDs to ensure precise alignment with the DRGs (Fig. 3b). These devices can be charged through a wireless closed-loop automatic charging system while the mice are housed in their home cages, allowing for unrestricted movement within the enclosure. Once the device is fully charged, the mouse can be placed in “any” experimental apparatus without the need for additional power transmission, and experiments can be conducted while the device continues to charge (Fig. 3c). In all cases, the operating parameters of the μ-LEDs (1-40 Hz, 0-1000 ms pulse width) can be wirelessly controlled via a custom smartphone application, and the battery level can be monitored in real-time through BLE communication. The OS device features a compact and lightweight electronic design (Fig. 3d), with a total weight of only 0.6875 grams (long, wide, thick, 16 × 8 × 4 mm, excluding the length of the wires and μ-LEDs), allowing for seamless integration into the bodies of rodents while enabling them to maintain natural behaviors and movements.

Figure 3e illustrates the circuit structure of the wireless charging system. This system is designed to operate at a resonant frequency of 6.78 MHz and employs a 6-turn coil with a 5 μH inductor, conforming to the standards set by the Alliance for Wireless Power (A4WP), which supports simultaneous wireless charging of multiple devices[32]. The antenna coil within the system utilizes inductive coupling technology to capture wireless energy, which is then rectified and boosted by a step-up converter to generate the voltage required for battery charging. To prevent accidental discharge of the battery, a Schottky diode is included in series with the battery at the load side of the circuit design. This design enables the wireless charging technology to

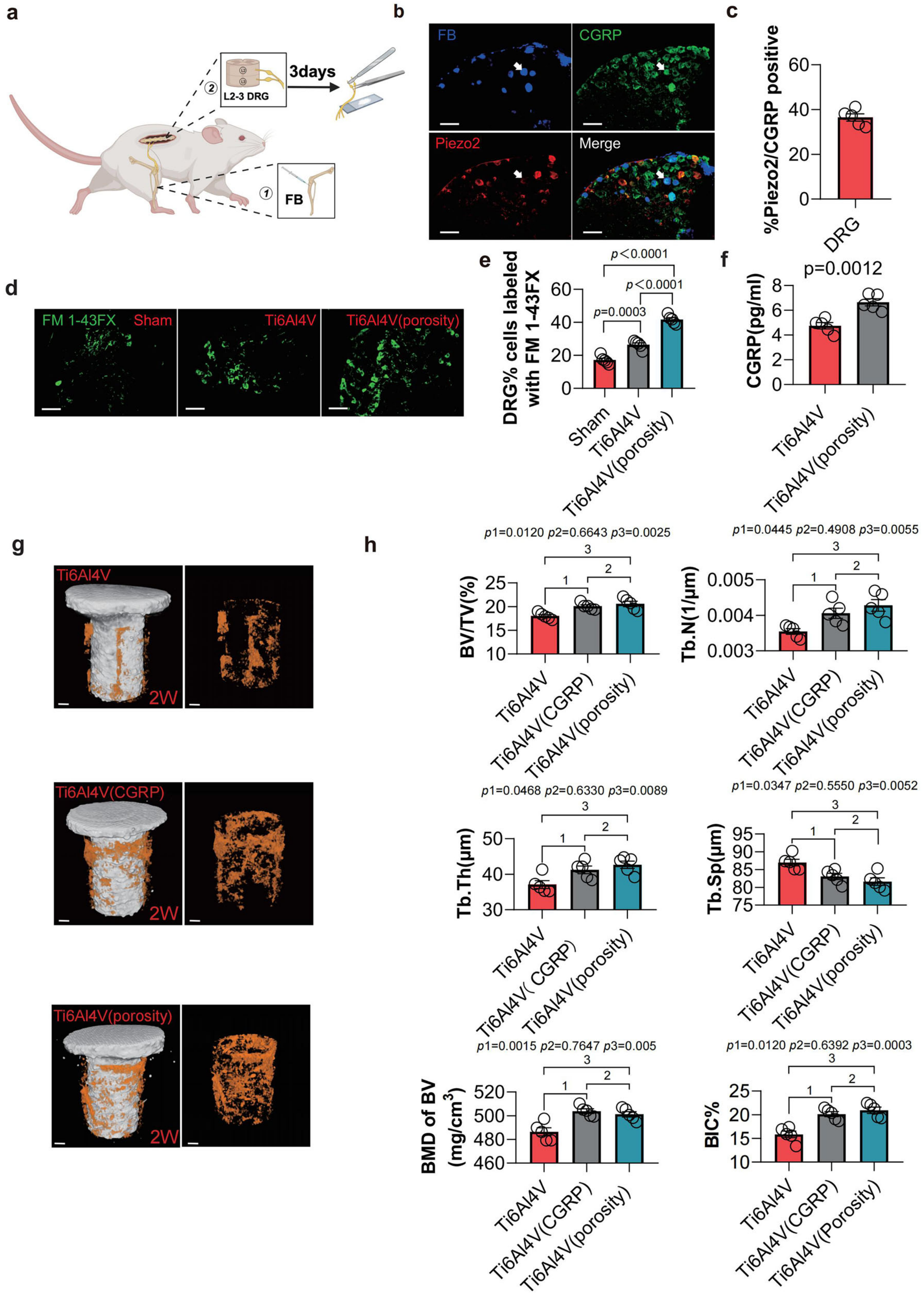

provide a stable DC power supply for the BLE SoC and μ-LEDs, ensuring reliable wireless communication and operation. The charging box for the optoelectronic system (Supplementary Fig. 3a) and the mobile terminal (Supplementary Fig. 3b) are both located externally. The charging box consists of a power supply interface (PSP), a main printed circuit board (PCB), and a heat dissipation module (HDM) (Supplementary Fig. 3c). Through a Bluetooth connection, the mobile terminal can coordinate the control of the main control chip of the optoelectronic system, thereby adjusting the operating parameters of the OS components. At the same time, the wireless charging achieves a small specific absorption rate (SAR < 0.12 W/kg) (Supplementary Fig. 3d). All materials and electronic components are commercially available and can be processed and assembled using standard manufacturing techniques.

Fig. 2 | The implantation of high elastic modulus implants leads to decrease CGRP levels released by Piezo2$^+$ nerves, FAK expression, and bone osseointegration. a Schematic diagram of L2-3 DRGs immunofluorescence staining performed 3 days after retrograde tracer FB intramedullary injection into the upper tibia (Created in BioRender. m*[POEj,m*. (2025) https://BioRender.com/h48v716). **b**, **c** Immunofluorescence staining and quantification of CGRP and Piezo2$^+$ neurons in DRG 3 days after implantation, scale bar: 100µm. Data are presented as mean ± SEM ($n = 5$ biologically independent experiments). **d**, **e** Immunofluorescence staining and quantification of FM1-43FX in DRG 24 hours after injection in sham and implant groups, scale bar: 100µm. Data are presented as mean ± SEM ($n = 5$ biologically independent experiments). *P*-values were calculated using one-way ANOVA with Tukey's multiple comparisons test. **f** ELISA detection of CGRP expression around the implants in the Ti6Al4V group and Ti6Al4V (Internal porosity) group one week postoperatively. Data are presented as mean ± SEM ($n = 5$ biologically independent experiments). *P*-values were calculated using Two-tailed Student's *t* tests. **g**, **h** Representative micro-CT images and quantitative analysis of peri-implant bone tissue at two weeks postoperatively in the Ti6Al4V group, Ti6Al4V+Inject CGRP group, and Ti6Al4V (Internal porosity) group, scale bar:100µm. Data are presented as mean ± SEM ($n = 5$ biologically independent experiments). *P*-values were calculated using one-way ANOVA with Tukey's multiple comparisons test. (FB:Fast Blue, CGRP: calcitonin gene-related peptide, BV/TV: bone volume/total volume, Tb.Th: trabecular thickness, Tb.N: number of trabeculae, Tb.Sp: trabecular spacing, BMD of BV: bone mineral density of bone volume, BIC%: bone-implant contact percentage). Source data are provided as a Source Data file.

Validation of the wireless optoelectronic system's performance and biocompatibility

To evaluate the optoelectronic performance of the OS device, we conducted a series of tests, including the device's operating voltage response and luminous output under different driving currents. Initially, we tested the voltage stability of the device when operated at a 5 mA driving current, 2 Hz frequency, and 10 ms pulse width for 30 minutes, finding that the operating voltage remained within the range of 2.8–3 V (Fig. 3f). By using in vitro activation of the OS device ($\lambda = 470$ nm), we assessed the voltage and output power response under various operating currents. The results indicated that at a 10 mA operating current and 3.0 V forward voltage, the optoelectronic system could output a power of 15 mW (Fig. 3g), sufficient to activate ChR2$^+$ neural axons[33]. We also monitored the temperature changes of the OS device in vivo, discovering that under an optogenetics density of 100 mW/mm^2 and a 25% duty cycle, the temperature increased by less than 2 °C after 30 minutes of operation; while at an optogenetics density of 80 mW/mm^2 and a 10% duty cycle, the temperature rise was less than 0.5 °C within 30 minutes (Fig. 3h). For wireless energy transmission, we utilized a charging case with an output power of 40 W and an effective charging range of up to 60 cm in circumference, the optogenetic device can be fully charged within 30 minutes when positioned above the charging box (Fig. 3i). Even with changes in the animal's posture affecting the device's position, the charging process remained rapid, at a distance of 22 cm above the charging box, the charging transmission efficiency reaches 49.015% (Fig. 3j). Once fully charged, the OS device could operate continuously for ~30 minutes (Fig. 3k).

The aforementioned experimental results demonstrate that this OS device is not only compact in size but also operates stably, making it suitable for targeted OS of the peripheral nervous system (PNS). To evaluate the potential impact of the OS device implantation on mice, we conducted a series of motor function tests on mice implanted with the device. Specifically, we compared the motor endurance and coordination of mice implanted with the OS device (Implanted group) to those of mice that underwent no surgery (Sham group). Two weeks post-implantation, the exploratory behavior, fatigue endurance, and motor coordination of the mice showed no significant differences (Supplementary Fig. 3e-h). Additionally, we found that the implantation of the OS device did not affect the mechanical sensitivity (Supplementary Fig. 3i) or heat sensitivity (Supplementary Fig. 3j) of the hind paw on the operated side. Further, immunohistochemical staining of liver, kidney, and spleen tissues revealed no adverse effects on the structure of these organs (Supplementary Fig. 4a). Blood sample analysis also indicated that the implantation had no significant impact on liver and kidney function markers (Supplementary Fig. 4b). Therefore, our biocompatibility assessment suggests that the OS device can be safely implanted near the DRG and can remain in place for extended periods.

OS of Piezo2$^+$ Nerves Promotes CGRP Release

ChR2 is a light-gated ion channel activated by blue light[34]. To specifically activate nociceptive neurons surrounding the implant, we crossed mice expressing ChR2-tdTomato with *Piezo2-Cre* driver mice, resulting in the generation of mice specifically expressing the photosensitive protein (Piezo2::ChR2) (Fig. 4a). Immunofluorescence staining confirmed the specific expression of ChR2 in the DRG, sciatic nerve, and tibia (Fig. 4b–d). To verify the activation of nociceptive nerve axons at the epineurium, we implanted the OS device around the L2-3 DRGs of Piezo2::ChR2 mice (Fig. 4e & Supplementary Fig. 5a) and conducted OS experiments 10 days later (10 mA, 10 ms, 2HZ, 30 min, Fig. 4f & Supplementary Fig. 5b), followed by testing mechanical and heat sensitivity. At the same time, we employed ES as a positive control. The results showed a significant increase in mechanical sensitivity immediately after OS and ES (Fig. 4g), while heat sensitivity did not significantly increase between with and without OS groups, However, ES group significantly increased heat sensitivity (Fig. 4h). We also generated Nav1.8::ChR2 mice targeting almost all nociceptive neuron populations[35] (Supplementary Fig. 5c), in which OS and ES groups increased both mechanical sensitivity (Supplementary Fig. 5d) and heat sensitivity (Supplementary Fig. 5e). Further, conditioned place preference (CPP) experiments revealed that Nav1.8::ChR2 mice exhibited significant aversive behavior after OS, spending significantly less time in the stimulation zone compared to the non-stimulation zone ($p < 0.01$, Supplementary Fig. 5f), whereas Piezo2::ChR2 mice showed significantly reduced place aversion behavior ($p < 0.01$, Fig. 4i). Control mice (*Piezo2-Cre*$^{-/-}$::ChR2$^{+/+}$) and (*Nav1.8-Cre*$^{-/-}$::ChR2$^{+/+}$) did not exhibit significant aversive responses to OS (Fig. 4i & Supplementary Fig. 5f).

The nociceptors plays a crucial role in regulating skeletal metabolism through the secretion of various neuropeptides, such as CGRP, SP (Substance P), NPY (Neuropeptide Y), and VIP (Vasoactive Intestinal Peptide)[36,37]. One week after OS, we measured the levels of these nociceptive neuropeptides in the bone tissue surrounding the upper tibial implants in mice. The experimental results showed that OS activation significantly increased the release of CGRP and SP, with CGRP showing the most prominent change, whereas the levels of other neuropeptides increased to some extent but without significant differences (Fig. 4j–m). These results suggest that more precise targeting of Piezo2$^+$ nerves within the bone achieves the activation and release of CGRP while significantly reducing the pain side effects compared to broad-spectrum nociceptor stimulation.

Activation of Piezo2$^+$ nerves promotes sustained CGRP release and implant osseointegration

Ten days following the implantation of OS elements at the L2-3 DRGs of Piezo2::ChR2 mice, a Ti6Al4V tibial implant model was established. The experimental mice were randomly divided into three groups: the non-OS group and the OS group, with the latter receiving OS (10 mA, 2 Hz, 10 ms, for 30 minutes/day). And the ES group(10 Hz, 10 V, 500 µs)[21]. Micro-CT results indicated that at 2- and 4 weeks post-surgery, the OS and ES group had significantly higher BV/TV, Tb.Th, Tb.N, BMD of BV, and BIC% compared to the Non_OS group, while the Tb.Sp in the OS and ES group was significantly lower than in the Non_OS group (Fig. 5a–d). Hard tissue section staining with methylene blue-acid

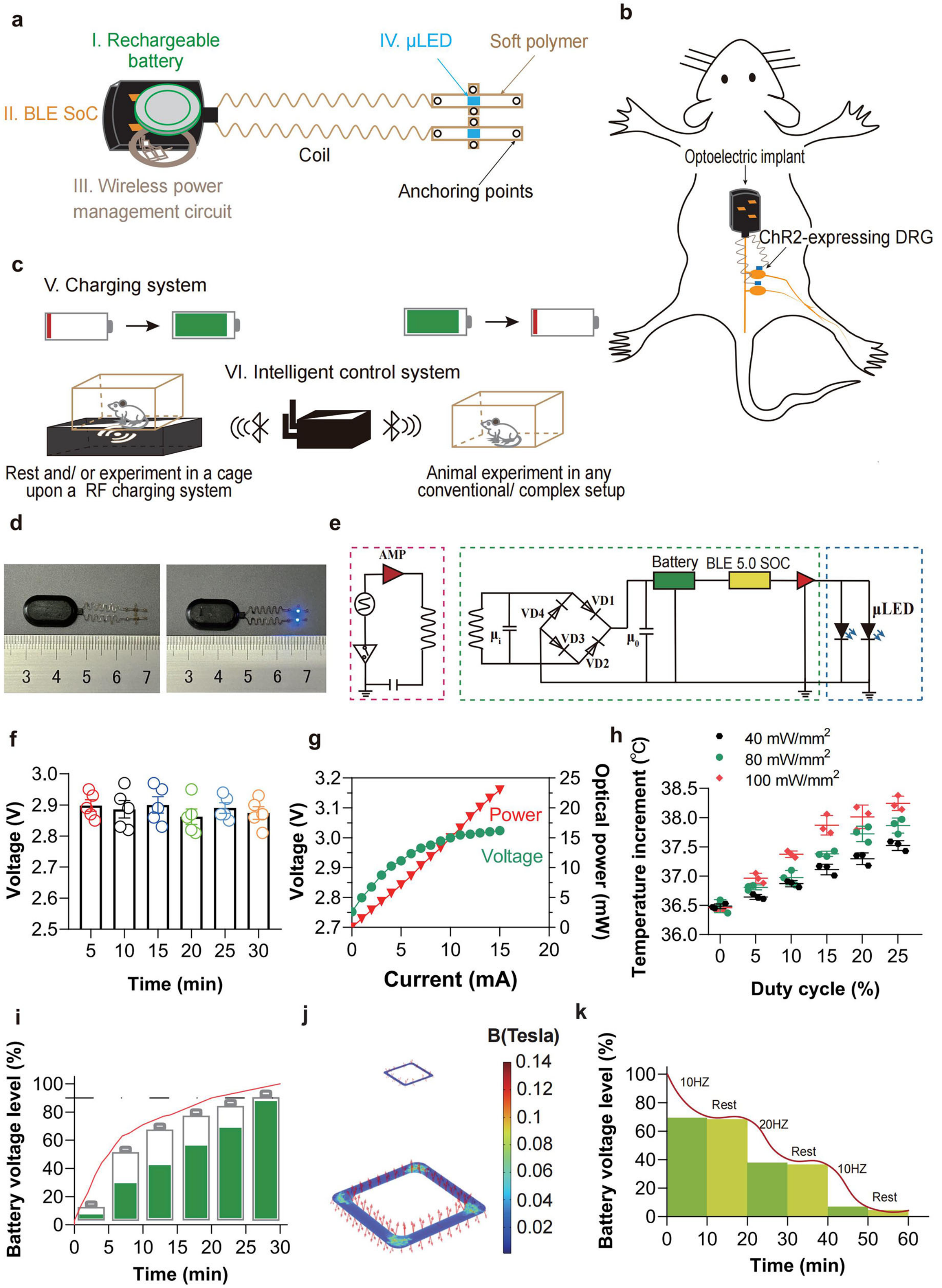

Fig. 3 | Design of a wireless, rechargeable, fully implantable OS device for stimulating mouse DRG. a Exploded view schematic of the wireless charging and smartphone-controlled OS device. **b** Schematic of the OS device implanted in a mouse to activate DRG. **c** Schematic of wireless charging for the implanted OS device. **d** The off and on photograph of the OS device. **e** Circuit diagram of the OS device. **f** Operating voltage of the OS device when running for 30 minutes at 5 mA drive current, 2 Hz frequency, and 10 ms pulse width. Data are presented as mean ± SEM (*n* = 5 biologically independent experiments). **g** Voltage and output power response of the OS device under different operating currents. **h** Temperature change of the OS device in vivo at different power levels. Data are presented as mean ± SEM (*n* = 3 biologically independent experiments). **i** Charging time of the optical stimulation component in proximity to the charging box. **j** Schematic diagram of spatial transmission efficiency for wireless charging (distance: 22 cm, transmission efficiency: 49.015%). **k** Discharging profile of the OS device. Source data are provided as a Source Data file.

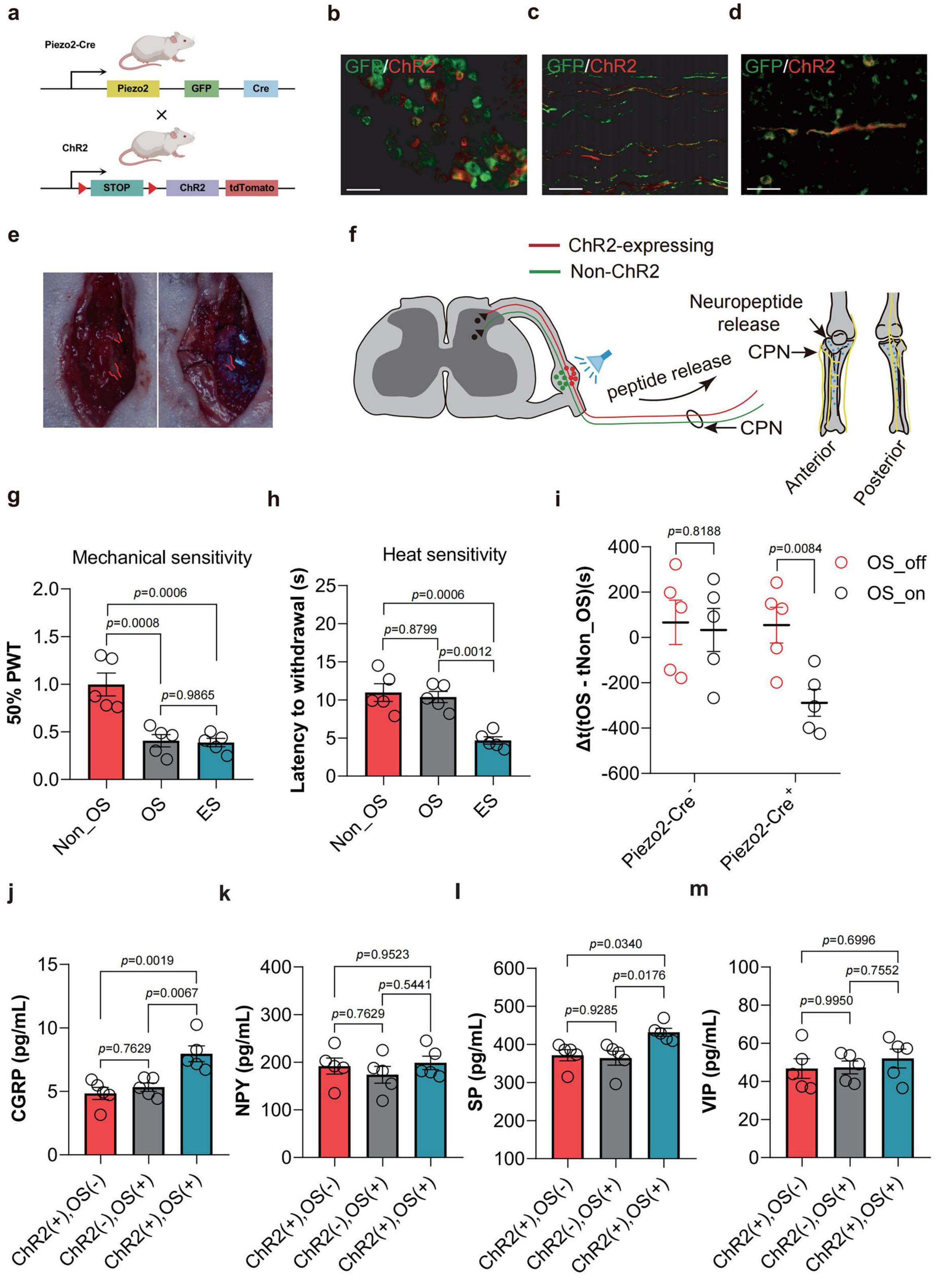

fuchsin revealed that at weeks 2 and 4, there was more new bone formation around the implants in the OS and ES group compared to the Non_OS group (Fig. 6a-d). Concurrently, the expression levels of CGRP in the surrounding bone tissue of the week 2 (Fig. 6e) and week 4 (Fig. 6f) OS and ES groups were significantly higher than those in the Non_OS group. Additionally, ALP staining (Supplementary Fig. 6a) of bone tissue around the implants at week 2 showed significantly higher ALP expression in the OS and ES groups compared to the Non_OS group (Supplementary Fig. 6b). Golden staining (Supplementary Fig. 6c) also indicated that type I collagen fiber formation around the implants was significantly increased in the OS and ES groups compared to the Non_OS group (Supplementary Fig. 6d). Further, at week 2 post-implantation, Western Blot (WB) results of key osteogenic proteins Runx2, ALP, OPN, and OCN in bone tissue around the implants from

Fig. 4 | OS of Piezo2$^+$ mechanical nociception promotes CGRP release. **a–d** Schematic diagram of Piezo2::ChR2 transgenic mouse construction and Piezo2 immunofluorescence staining in DRG, sciatic nerve, and tibial upper bone tissue, scale bar: 100 μm. (4a Created in BioRender. m*[POEj,m*. (2025) https://BioRender.com/h48v716). **e**, **f** Diagram of the OS device implanted around the DRG and the release of neuropeptides in the target area caused by OS of DRG in mice expressing ChR2. **g** Changes in mechanical sensitivity in Piezo2::ChR2 mice under OS. Data are presented as mean ± SEM (n = 5 biologically independent experiments). P-values were calculated using one-way ANOVA with Tukey's multiple comparisons test. **h** Changes in heat sensitivity in Piezo2::ChR2 mice under OS. Data are presented as mean ± SEM (n = 5 biologically independent experiments). P-values were calculated using one-way ANOVA with Tukey's multiple comparisons test. **i** Changes in aversive behavior in *Piezo2-Cre*$^+$ and *Piezo2-Cre*$^-$ mice under OS. Data are presented as mean ± SEM (n = 5 biologically independent experiments). P-values were calculated using Two-tailed Student's t tests. **j–m** ELISA experiment of neuropeptide release in the DRG target area of Piezo2::ChR2 mice under OS. Data are presented as mean ± SEM (n = 5 biologically independent experiments). P-values were calculated using one-way ANOVA with Tukey's multiple comparisons test. (ChR2: channelrhodopsin-2, CGRP: calcitonin gene-related peptide, SP: Substance P, NPY: neuropeptide Y, VIP: vasoactive intestinal peptide). Source data are provided as a Source Data file.

the Non_OS, OS and ES groups (Supplementary Fig. 6e) showed that the expression levels of bone formation-related proteins were significantly higher in OS and ES groups compared to that of Non_OS group (Supplementary Fig. 6f).

These results suggest that OS of Piezo2$^+$ DRG induces CGRP release, promoting tibial implant osseointegration by enhancing osteogenesis. The CGRP may influence the expression of inflammatory cytokines, and the inflammatory response also plays significant roles in osseointegration. To further verify their roles in OS-mediated osseointegration, we collected bone tissue surrounding the implants from the Non_OS, OS and ES groups two weeks post-surgery and performed ELISA assays for important inflammatory proteins (IL-1β, IL-6, IL-10, and TGF-β). We found a statistically significant difference in the expression of the inflammatory protein IL-10 when comparing the OS and ES groups to the Non_OS group, while no statistically significant differences were observed for the other inflammatory proteins (Supplementary Fig. 7a-d). Previous literature has reported that CGRP induces the expression of the anti-inflammatory cytokine IL-10[38], but the effect of IL-10 on osseointegration may not be significant.

The indispensable role of CGRP-activated FAK in OS of mechanosensory nerves to enhance osseointegration

Bone formation or regeneration requires the recruitment, proliferation, and osteogenic differentiation of stem cells/stromal cells, with mechanical weighting being a potent stimulus driving this process[39]. BMSCs can sense mechanical signals and activate osteogenic signaling pathways, thereby upregulating the expression of relevant osteogenic genes[40]. Interestingly, BMSCs express the CGRP receptor RAMP1[41], allowing them to be regulated by nociceptor neurotransmitters. To further elucidate whether OS activation of nociceptors enhances osseointegration of implants by promoting the osteogenic differentiation of BMSCs, we isolated and primary cultured DRGs of Piezo2::ChR2 mice and subjected them to culture conditions with or without OS (Fig. 7a). The conditioned media from both groups of DRGs were then added to osteogenic induction media. WB analysis after one week of co-culture with Ti6Al4V implant material and BMSCs (Fig. 7b) showed significantly elevated FAK phosphorylation levels in the OS group (Fig. 7c). Simultaneously, we conducted transcriptome sequencing on two groups of BMSCs one week post-culture. The heatmap (Supplementary Fig. 8a) revealed that the expression of Ptk2, which encodes FAK, was significantly elevated in the OS group. GO enrichment analysis (Supplementary Fig. 8b) highlighted terms related to ossification and response to stimulus. Additionally, KEGG enrichment analysis (Supplementary Fig. 8c) identified increased expression in stress-related pathways, including focal adhesion and Hippo signaling. Similarly, GSEA showed an increase in nucleosome-dependent ATPase activity associated with mechanical stress (Supplementary Fig. 8d). Additionally, BMSCs were co-cultured with the implant materials. SEM results (Fig. 7d) indicated more BMSCs adhesion on the surface of the implant material in the OS group (Fig. 7e). And in a pure BMSCs osteogenic induction culture system. ALP staining of BMSCs after two weeks of culture (Fig. 7f) showed significantly higher ALP expression in the OS group compared to the Non_OS group (Fig. 7g). Further, Alizarin Red staining after three weeks of culture (Fig. 7h) revealed markedly enhanced calcium nodule formation in the OS group compared to the Non_OS group (Fig. 7i), indicating increased activity of early osteogenic markers. Additionally, immunofluorescence staining of ALP, Runx2, OPN, and OCN after two weeks of BMSCs culture (Supplementary Figs. 9a, c, e, g) and semi-quantitative analysis demonstrated significantly elevated levels of ALP, RUNX2, OPN, and OCN expression in the OS group on day 14 (Supplementary Figs. 9b, d, f, h). We performed RT-PCR analysis of CGRP and FAK expression in the surrounding tissues of the implant from both the OS and Non-OS groups at 0–21 days. The results revealed that the expression level of CGRP was higher in the OS group compared to the Non_OS group (Supplementary Fig. 10a), and the peak expression of FAK occurred earlier in the OS group (14 days vs. 7 days) (Fig. S10b). These results suggest that OS of DRGs promotes the osteogenic differentiation of BMSCs via CGRP/FAK pathway. Osteoclasts are also one of the important factors affecting osseointegration, in order to determine whether they are affected by the increased secretion of CGRP caused by OS, we conducted in vitro experiments to induce osteoclasts from bone marrow macrophages (BMMs). After six days of culture, TRAP staining showed that the supernatant of Piezo2::ChR2 mice's DRG did not affect osteoclast differentiation with or without OS (Supplementary Fig. 11a–b).

RAMP1 and CALCRL form a G protein-coupled receptor that signals through Gαs, leading to elevated levels of the second messenger cyclic AMP and activation of cAMP-dependent protein kinase PKA[42]. To determine whether OS of DRGs promotes FAK activation via CGRP release and whether this is regulated through the aforementioned pathway, we employed the CGRP receptor antagonist BIBN4096[43], the PKA inhibitor Rp-8-CPT-cAMP[44], and the FAK inhibitor Y15[20] to investigate the optogenetically induced effects on osseointegration. Micro-CT analysis two weeks post-implantation of tibial implants in Piezo2::ChR2 mice revealed that the OS group exhibited a more robust bone structure surrounding the implant than Non_OS group (Fig. 8a). Quantitative micro-CT data indicated significant increases in BV/TV, Tb.N, Tb.Th, BMD of BV, and BIC% in the OS group, while Tb.Sp was decreased; these effects were inhibited by BIBN4096, Rp-8-CPT-cAMP, and Y15 (Fig. 8b). Further, by evaluating the expression levels of key osteogenic proteins RUNX2, ALP, OPN, and OCN in the tissue surrounding the implants (Fig. 8c), semi-quantitative analysis showed the highest expression of these proteins in the OS group, an effect that was inhibited by BIBN4096, Rp-8-CPT-cAMP, and Y15 (Fig. 8d). Our previous results indicated that OS of Piezo2::ChR2 mice significantly increased the release of SP in the targeted region of the DRG. To further validate the role of SP in the enhancement of osseointegration through OS, we intervened with the SP receptor antagonist L-733060, using C57BL/6 mice as negative controls. Two weeks later, micro-CT analysis revealed that L-733060 did not inhibit osseointegration, and the OS of C57BL/6 mice did not promote osseointegration (Supplementary Fig. 12a–b). Similarly, methylene blue-acid red staining of hard tissue sections two weeks post-treatment yielded consistent results (Supplementary Fig. 12c, d). These results suggest that the promotion of osseointegration by Piezo2$^+$ neurons depends on the activation of the CGRP-PKA-FAK signaling axis than the SP signaling axis.

Discussion

In this study, we found that high-modulus implants induce stress shielding, which suppresses the expression of IMM FAK in BMSCs surrounding the implant, and is associated with a reduction in the

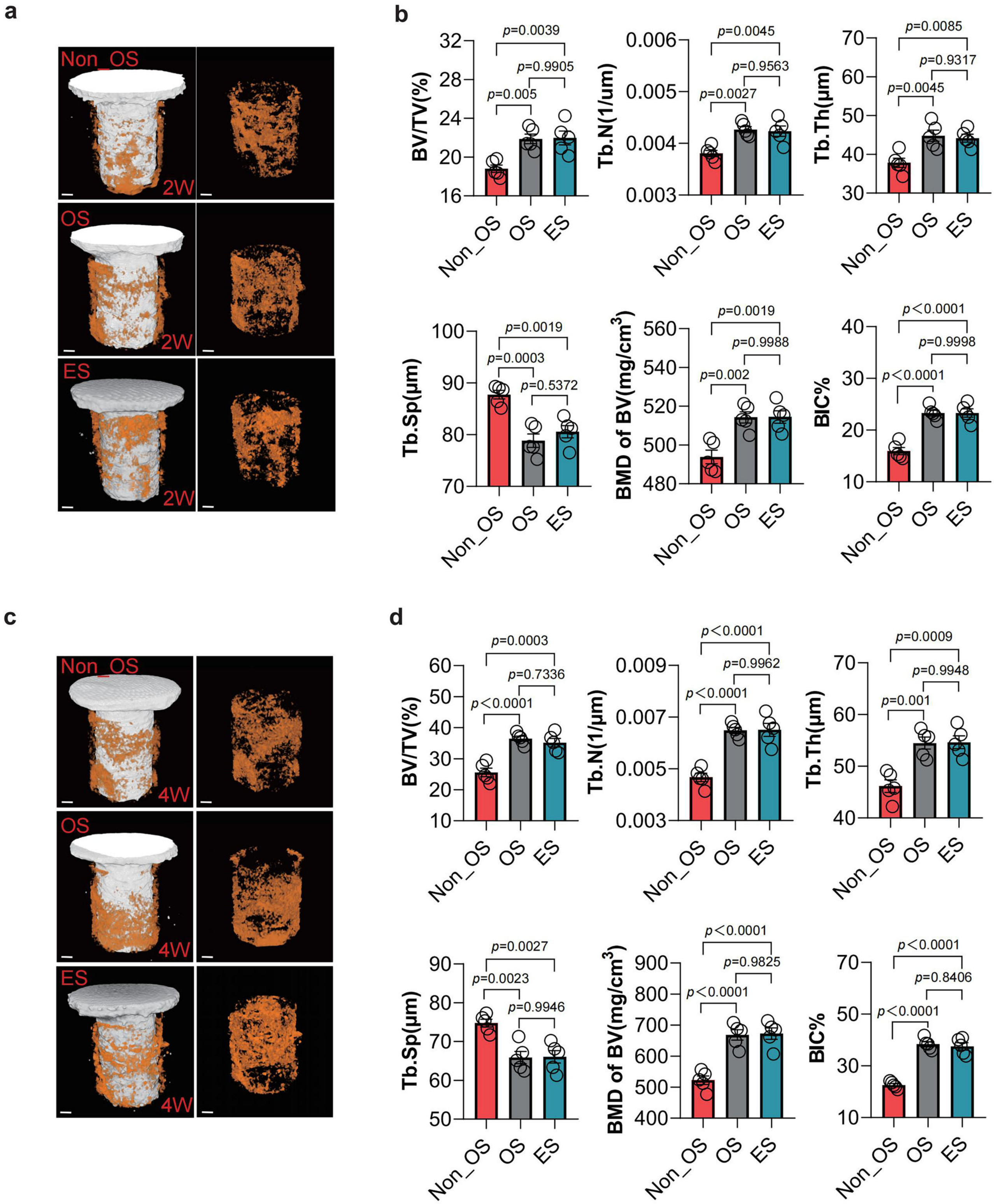

Fig. 5 | Stimulation of Piezo2$^+$ mechanical nociception promotes implant osseointegration. a–d micro-CT images and quantitative analysis of bone tissue surrounding implants were conducted in Piezo2::ChR2 mice across Non_OS, OS and ES groups, at 2 and 4 week post-implantation, scale bar: 100 μm. Data are presented as mean ± SEM (n = 5 biologically independent experiments). P-values were calculated using one-way ANOVA with Tukey's multiple comparisons test. (BV/TV: bone volume/total volume, Tb.Th: trabecular thickness, Tb.N: number of trabeculae, Tb.Sp: trabecular spacing, BMD of BV: bone mineral density of bone volume, BIC%: bone-implant contact percentage). Source data are provided as a Source Data file.

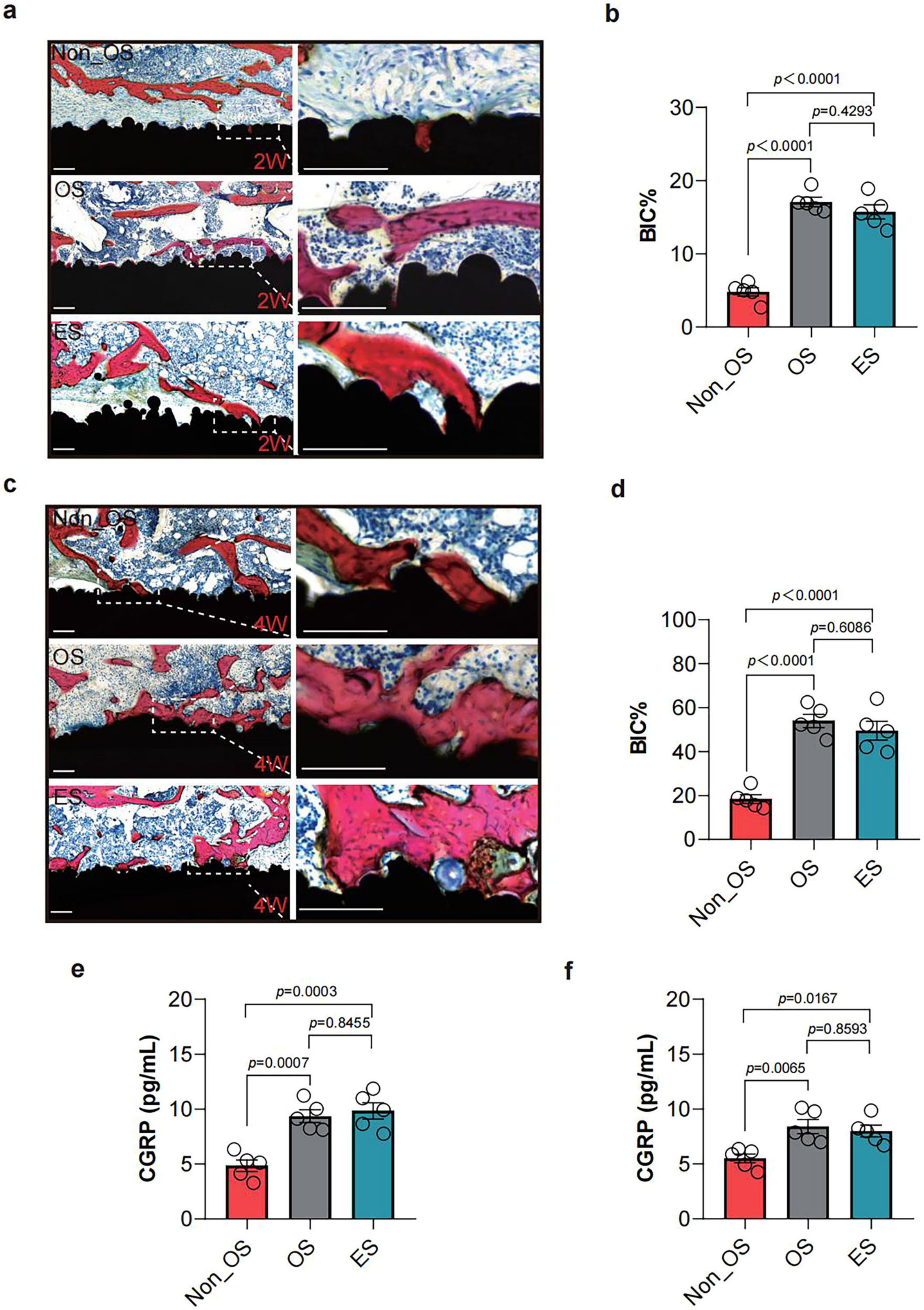

Fig. 6 | OS of Piezo2$^+$ mechanical nociception promotes implant osseointegration. a–d Methylene blue-acid fuchsin staining images and semi-quantitative analysis of bone tissue containing implants in Piezo2::ChR2 mice, with and without OS and ES, at 2 and 4 week post-implantation, scale bar: 10×: 100 µm, 40×: 100 µm. Data are presented as mean ± SEM ($n = 5$ biologically independent experiments). *P*-values were calculated using one-way ANOVA with Tukey's multiple comparisons test. **e–f** ELISA detection of CGRP expression levels in bone tissue surrounding implants in Piezo2::ChR2 mice, with and without OS and ES, at 2 and 4 week post-implantation. Data are presented as mean ± SEM ($n = 5$ biologically independent experiments). *P*-values were calculated using one-way ANOVA with Tukey's multiple comparisons test. Source data are provided as a Source Data file.

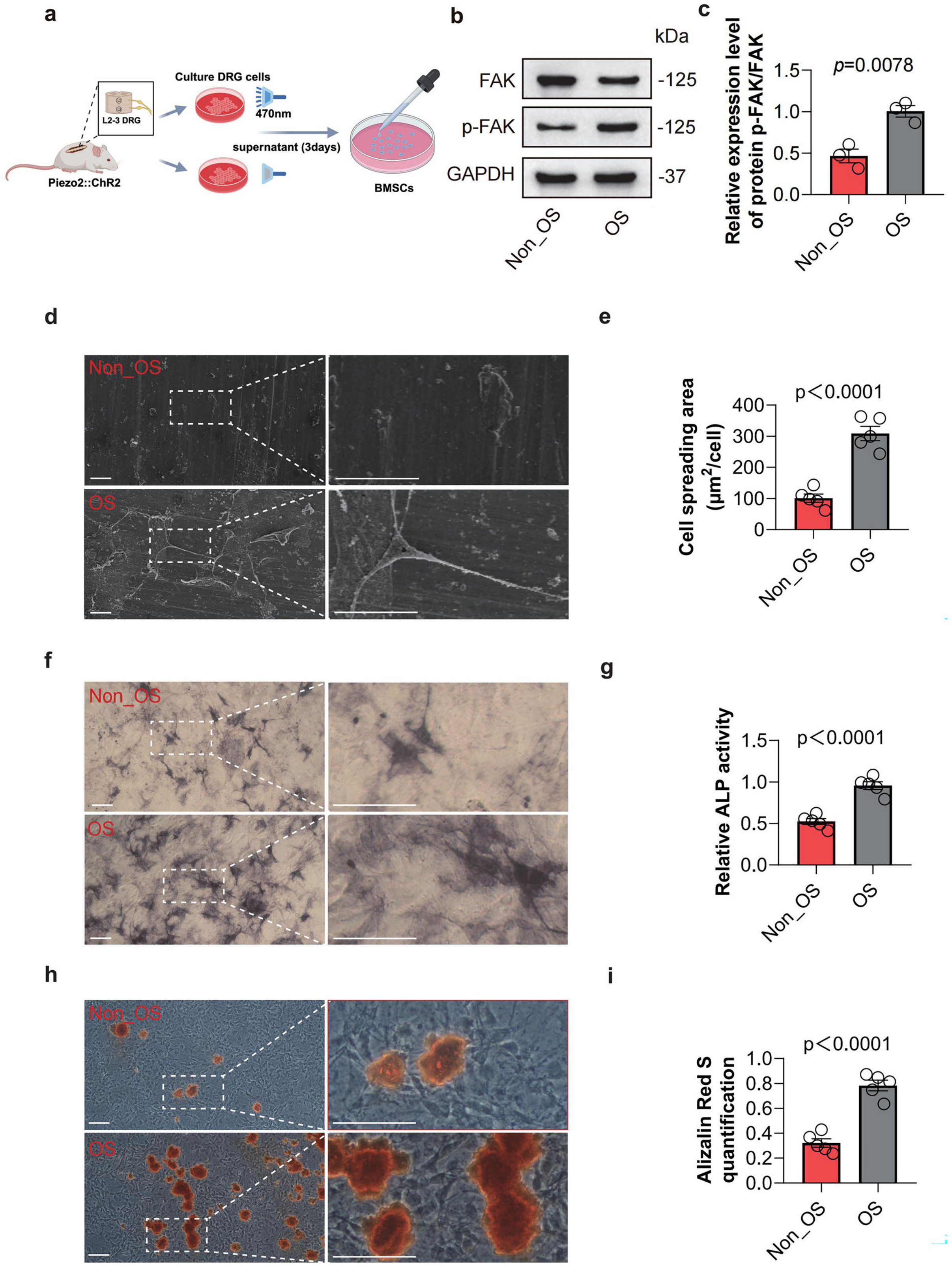

secretion of CGRP by mechanosensitive Piezo2$^+$ fibers within the bone. We designed an implantable, wirelessly rechargeable OS targeting Piezo2$^+$ DRGs. This continuous OS upregulated the biosynthesis and release of CGRP in the bone region surrounding the implant. This endogenous upregulation of CGRP reversed the suppression of FAK expression in BMSCs, thereby enhancing the osseointegration of tibial implants by promoting the osteogenic differentiation of BMSCs. In summary, the OS activation in L2-3 DRGs of mice expressing ChR2 in mice facilitates the targeted release of CGRP onto the RAMP1-CALCRL receptor on BMSCs surrounding the tibial implant, promoting PKA expression, enhancing the elevated expression and phosphorylation of FAK, and driving the differentiation of BMSCs into osteoblasts. This enhances the osseointegration of the implants. We propose a concept for the precise targeting and minimally invasive stimulation of

Fig. 7 | Stimulation of Piezo2$^+$ mechanical nociception promotes CGRP release, activates FAK expression, and enhances osteogenic differentiation of BMSCs. **a** Schematic diagram of BMSCs culture with the addition of supernatant from DRGs of Piezo2::ChR2 mice under both with and without OS. (Created in BioRender. m*[POEj,m*. (2025) https://BioRender.com/h48v716). **b**, **c** WB detection and semi-quantitative analysis of FAK levels in BMSCs in a Ti6Al4V implant material BMSCs co-culture system after 7 days, with and without the addition of OS DRG supernatant (The samples derive from the same experiment and that blots were processed in parallel). Data are presented as mean ± SEM (n = 3 biologically independent experiments). P-values were calculated using Two-tailed Student's t tests. **d**, **e** SEM images and semi-quantitative analysis of the Ti6Al4V implant material BMSCs co-culture system after 7 days, with and without the addition of OS DRG supernatant, scale bar: 100 µm. Data are presented as mean ± SEM (n = 5 biologically independent experiments). P-values were calculated using Two-tailed Student's t tests. **f**, **g** In a pure BMSC osteogenic induction culture system, ALP staining and semi-quantitative analysis of BMSCs in osteogenic induction culture with and without the addition of OS DRG supernatant after 14 days, scale bar: 100 µm. Data are presented as mean ± SEM (n = 5 biologically independent experiments). P-values were calculated using Two-tailed Student's t tests. **h**, **i** In a pure BMSC osteogenic induction culture system, ARS staining and semi-quantitative analysis of BMSCs in osteogenic induction culture with and without the addition of OS DRG supernatant after 21 days, scale bar: 100 µm. Data are presented as mean ± SEM (n = 5 biologically independent experiments). P-values were calculated using Two-tailed Student's t tests. (FAK: focal adhesion kinase; ALP: alkaline phosphatase). Source data are provided as a Source Data file.

mechanosensitive nerves to address the clinical issue of inadequate osseointegration resulting from stress shielding induced by implants.

Mechanical stress plays a crucial role in the osseointegration of implants. When implants with a modulus higher than that of bone are used, the majority of the mechanical load is absorbed by the metal, thereby inhibiting the transmission of stress to the bone at the implant-bone interface. This study demonstrates that the primary effect of this inhibition is the suppression of FAK expression. FAK is a key structure in cell-extracellular matrix adhesion and plays a significant role in the transduction of mechanical signals[45,46]. When pressure is applied to FAK, the protein undergoes a conformational change that recruits additional FAK protein, thereby enhancing functions such as osteoblastic differentiation, migration, and mineralization[47]. Current research primarily focuses on the enhancement of implant materials and the improvement of implant surface properties through physical means to promote osseointegration to a certain extent[48]. Among these, biodegradable metals represent a prominent direction of research and application. Biodegradable metals exhibit mechanical properties that are compatible with natural bone, thereby reducing "stress shielding"[49]. Furthermore, the gradual degradation of these metals within the body results in the release of metallic ions, such as magnesium, which can stimulate the release of relevant neuropeptides. This, in turn, promotes the proliferation, differentiation, and mineralization of osteogenic-related cells, thereby accelerating bone healing[20,49,50]. The inspiration drawn from the aforementioned exemplary studies is that neuropeptides may serve as one of the mechanisms to promote the osseointegration of implants. However, directly stimulating the cells at the bone-implant interface to modulate FAK expression post-implantation poses significant challenges[51].We propose a strategy that employs optogenetics to modulate the mechanosensitive nerves in the microenvironment of BMSCs, thereby promoting the upregulation of FAK expression. This approach serves as a complementary enhancement to existing material improvements, broadening its application scenarios, and can be integrated with material enhancement strategies to further facilitate osseointegration of implants. For instance, it may serve as an adjunctive intervention in cases where the implantation surgery has been completed but osseointegration is inadequate[51,52].

Due to the opacity of the peripheral nerve system (PNS) epineurium and the activity of limb nerves while the animal is awake, directly stimulating the axons of peripheral nerves presents significant challenges. Bone tissue is intricately connected with DRG and the central nervous system (CNS) through extensive sensory nerve innervation. The apply of DRG stimulation instead of PNS axons stimulation is a compromise to achieve the research purpose under the existing technical conditions[21]. Building upon this foundation, we introduced OS techniques to achieve precise targeting and activation of mechanosensitive DRG, a method that has predominantly been utilized for stimulating CNS neurons in previous studies[53]. Recent advancements in miniaturization technologies and material science have facilitated the integration of optogenetics and optoelectronic systems into the PNS[54,55].This is crucial for conducting long-term, precise behavioral studies in freely moving subjects[56]. Currently, there are two primary approaches: battery-based or battery-free systems. Battery-based systems employ advanced SoC electronic devices and BLE, necessitating the installation of external equipment on the animals' heads[57]. This increases the weight of the experimental animals' heads, potentially restricting their mobility. Battery-free fully implanted systems transmit energy and control signals via magnetic field inductive coupling, presenting an appealing solution to mitigate postoperative and long-term interventions in animal models. However, this approach necessitates the use of specially designed cages with integrated transmission antennas, facing challenges such as uneven magnetic field distribution and restricted usage scenarios[58]. In light of these challenges, we have designed a wireless, rechargeable, fully implantable OS device. This device is positioned on the animal's back, facilitating near-field magnetic resonant coupling for charging at distances of several tens of centimeters, thereby allowing the experimental animals to move freely within an unrestricted environment. Compared to previous studies[24], this OS device is smaller in size and lighter in weight, with a flexible and adjustable wire connected to the µ-LEDs, which facilitates precise alignment of the µ-LEDs with the surrounding neural stimulation sites. To our knowledge, this represents a fully implantable, wirelessly rechargeable optogenetic stimulation device specifically developed for use in mice.

Currently, there are various methods targeting nociceptive nerves to promote the release of endogenous neuropeptides[59,60]. Although these methods have shown promising effects in disease modulation, the activation of nociceptors inevitably induces pain, making it crucial to minimize this side effect for clinical applications. Nociceptors exist in several subtypes. This study found that it is not necessary to broadly stimulate NAV1.8$^+$ and TRPV1$^+$ nociceptors; instead, targeting Piezo2$^+$ mechanosensitive nerves can achieve the same neuropeptide release and FAK regulation effects with significantly reduced pain sensitization. This finding holds substantial significance for future applications.

There is substantial literary indicating that neuropeptides mediate crosstalk between neurons and osteoblastic lineage cells, such as BMSCs, osteoblasts, and osteocytes[61,62]. The overall effect tends to promote osteogenesis. Some research suggests that FAK activation depends on the cAMP-PKA signaling pathway[63]. Based on this background, we discovered that CGRP enhances BMSC FAK expression by activating the G protein-coupled receptor formed by Ramp1 and its coreceptor CALCRL[42], mediated through adenylate cyclase-induced cAMP and PKA signaling. Understanding this pathway may aid in the development of future targeted methods for stimulating IMM derived from nociceptive neurons.

Our study has certain limitations. We measured the expression levels of four key inflammatory proteins and observed differences in IL-10 expression between the two groups. However, we have not conducted further investigations into its role in promoting targeted osseointegration at the DRG site under OS. Future studies are essential

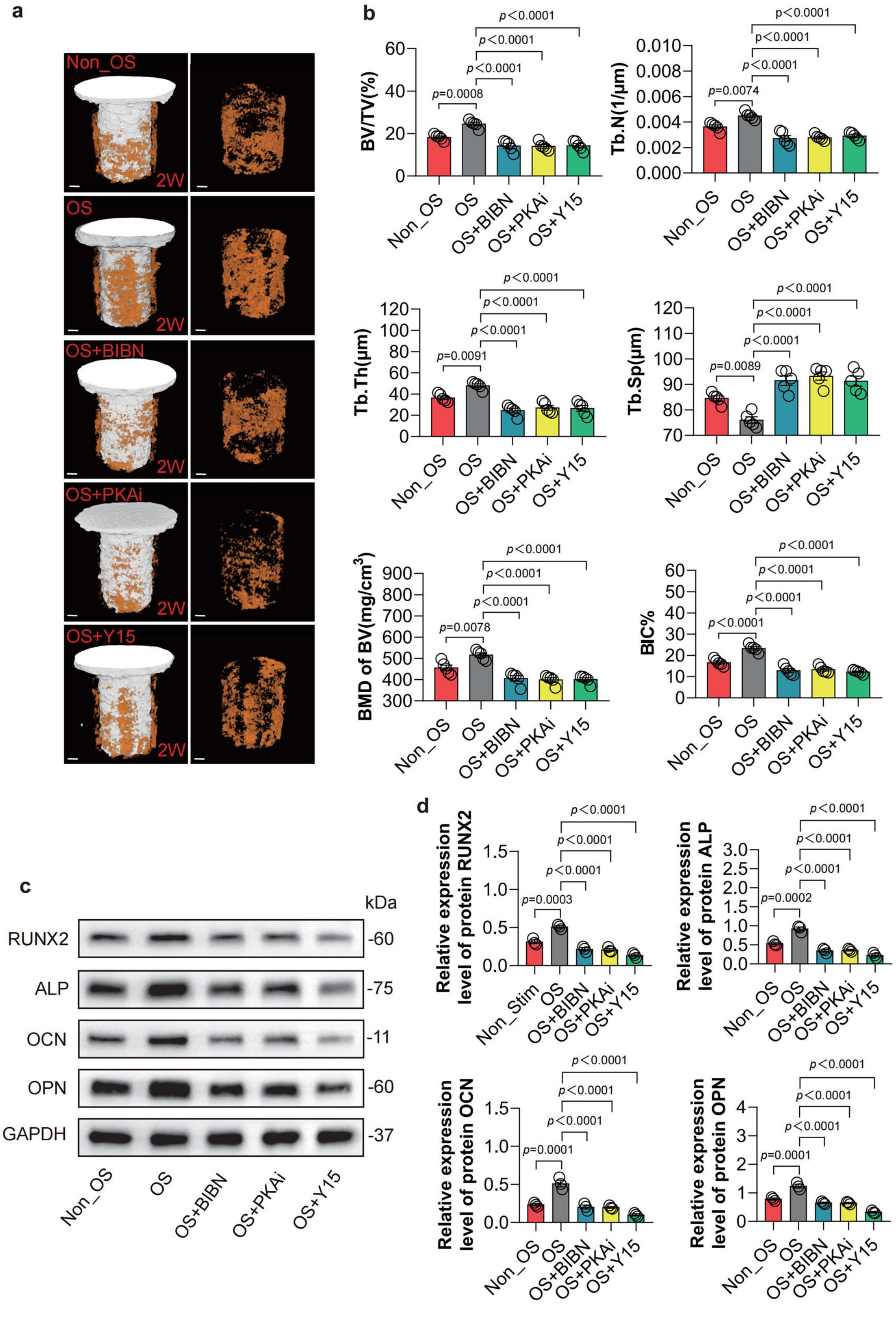

to elucidate its potential mechanisms of action. Additionally, the extra lumbar surgery utilized to stimulate the DRG introduce a degree of procedural trauma. In future research, the use of non-virulent viruses for the expression of light-sensitive ion channel proteins in neurons, the application of vascular nano-transport techniques[64] for virus delivery to avoid invasive procedures on the nerves, and ongoing improvements in optogenetic devices are expected to enable the development of a non-surgical, non-invasive, and highly precise method for peripheral nerve stimulation.

Overall, the mechanical elastic modulus of implants significantly influences osseointegration, involving multiple complex biomechanical and biochemical mechanisms. Given that the elastic modulus of current orthopedic implants cannot fully match that of bone for weight-bearing functions[7], we have adopted a strategy of targeting

Fig. 8 | OS of Piezo2^{+} mechanical nociception promotes implant osseointegration by activation of CGRP-PKA-FAK signaling pathway. a, **b** Micro-CT images and quantitative analysis of the bone tissue surrounding the implants after 2 weeks of treatment with different antagonists/inhibitors, scale bar: 100 μm. Data are presented as mean ± SEM (n = 5 biologically independent experiments). P-values were calculated using one-way ANOVA with Tukey's multiple comparisons test. **c**, **d** Expressin levels and semi-quantitative analysis of osteogenesis-related proteins (Runx2/ALP/OPN/OCN) in the bone tissue surrounding the implants after 2 weeks of treatment with different antagonists/inhibitors (The samples derive from the same experiment and that blots were processed in parallel). Data are presented as mean ± SEM (n = 5 biologically independent experiments). P-values were calculated using one-way ANOVA with Tukey's multiple comparisons test. (ALP: alkaline phosphatase, Runx2: recombinant Runt related transcription factor 2, OPN: osteopontin, OCN: osteocalcin, GAPDH: glyceraldehyde-3-phosphate dehydrogenase, BV/TV: bone volume/total volume, Tb.Th: trabecular thickness, Tb.N: number of trabeculae, Tb.Sp: trabecular spacing, BMD of BV: bone mineral density of bone volume, BIC%: bone-implant contact percentage). Source data are provided as a Source Data file.

mechanosensitive nociceptors to promote the expression of IMM in BMSCs around the prosthesis, thereby enhancing osseointegration. This offers a biological regulation method for the field, utilizing the modulation of endogenous neuropeptides to improve bone-implant integration. However, the mechanisms by which various cells within bone tissue interact with the sensory nervous system to mediate osseointegration are highly complex[48]. Our understanding of this field remains limited, particularly regarding how to more precisely regulate the secretion of specific subtypes of mechanosensitive neuropeptides without causing additional side effects.

Methods

Ethical statement

The Animal Experiment Ethics Committee of Fujian Medical University has approved all experimental protocols (Approval No. IACUC FJMU 2023-Y-0535), which comply with international standards.

Mice

The animals were housed in individually ventilated cages at a temperature of 22–24 °C, humidity of 60 ± 5%, and a 12-hour light/dark cycle, with unrestricted access to water and food. Healthy male mice aged 8–14 weeks were used in this study. Euthanasia of the animals was performed using carbon dioxide. C57BL/6 J mice were purchased from Beijing HFK Bioscience Co., Ltd. C57BL/6JSmoc-*Trpv1*$^{em1(Myc\text{-}IRES\text{-}Cre)Smoc}$ (NM-KI-200139), C57BL/6Smoc-*Piezo1*$^{tm2(CreERT2)Smoc}$ (NM-KI-18048) and C57BL/6Smoc-Gt(ROSA)26Sor$^{em1(CAG\text{-}LSL\text{-}ChR2(H134R)\text{-}tdTomato\text{-}WPRE\text{-}polyA)Smoc}$ (NM-KI-190113) mice were purchased from Shanghai Biomodel Organism Science and Technology Development Co., Ltd. B6(SJL)-*Piezo2*$^{tm1.1(cre)Apat}$/J (JAX 027719), C57BL/6-*Gt(ROSA)26Sor*$^{tm1(HBEGF)Awai}$/J (JAX 007900) and B6.129P2-*Gt(ROSA)26Sor*$^{tm1(DTA)Lky}$/J (JAX 009669) mice were purchased from Jackson Laboratories. *Nav1.8-Cre* mice were provided by Professor Qiufu Ma (Harvard Medical School, Boston) and Professor Longzhen Cheng (Southern University of Science and Technology, Shenzhen). C57BL/6JSmoc-*Trpv1*$^{em1(Myc\text{-}IRES\text{-}Cre)Smoc}$ and B6(SJL)-*Piezo2*$^{tm1.1(cre)Apat}$/J heterozygous mice were bred with C57BL/6-Gt(ROSA) 26Sor$^{tm1(HBEGF)Awai/J}$ (JAX 007900) homozygous mice to generate *Trpv1-Cre*/DTR (*Trpv1-Cre*$^{+/-}$-DTR$^{+/-}$) and *Piezo2-Cre*/DTR (*Piezo2-Cre*$^{+/-}$-DTR$^{+/-}$) mice and littermate control mice (*Trpv1-Cre*$^{-/-}$-DTR$^{+/-}$ and *Piezo2-Cre*$^{-/-}$-DTR$^{+/-}$). C57BL/6Smoc-*Piezo1*$^{tm2(CreERT2)Smoc}$ heterozygous mice were bred with B6.129P2-*Gt(ROSA)26Sor*$^{tm1(DTA)Lky}$/J homozygous mice to generate *Piezo1-Cre*/DTA (*Piezo1-CreERT*$^{+/-}$-DTA$^{+/-}$) mice as well as littermate control mice (*Piezo1-CreERT*$^{-/-}$-DTA$^{+/-}$). B6(SJL)-*Piezo2*$^{tm1.1(cre)Apat}$/J and *Nav1.8-Cre* heterozygous mice were bred with C57BL/6Smoc-Gt(ROSA)26Sor$^{em1(CAG\text{-}LSL\text{-}ChR2(H134R)\text{-}tdTomato\text{-}WPRE\text{-}polyA)Smoc}$ homozygous mice to generate *Piezo2-Cre*/ChR2 (*Piezo2-Cre*$^{+/-}$-ChR2$^{+/-}$) and *Nav1.8-Cre*/ChR2 (*Nav1.8-Cre*$^{+/-}$-ChR2$^{+/-}$) mice or into littermate control mice (*Piezo2-Cre*$^{-/-}$-ChR2$^{+/-}$ and *Nav1.8-Cre*$^{-/-}$-ChR2$^{+/-}$). To ablate local Trpv1^{+} or Piezo2^{+} nociceptors in the bone surrounding the implant in *Trpv1*-Cre/DTR and *Piezo2*-Cre/DTR mice, DTX (10 ng/1 μL, ITI BioChem, ITI011691) was administered in the tibial intramedullary cavity prior to implant placement. Similarly, to ablate local Piezo1^{+} nociceptors in the same region in *Piezo1-Cre*/DTA mice, (Z)-4-hydroxytamoxifen (4-OHT, 20 μg/1 μL, Sigma–Aldrich, Cat. No. H7904) was administered before implant placement.

Tibial Implantation Model

Mice were anesthetized using a precision vaporizer with 2–3% isoflurane and the hair around the knee joint of the hind limb was completely removed. Following disinfection with povidone-iodine and draping, a skin incision was made along the midline of the knee joint. A lateral parapatellar approach was used to expose the knee joint, and the patella was displaced medially. The anterior cruciate ligament was transected to expose the tibial plateau. A reamer was used to prepare the tibia, and the tibial implant was inserted. The knee joint and patella were repositioned, and the joint incision was closed with interrupted 4-0 PGA sutures (PGA 4-0 sutures, Jinbei, China). The area was disinfected again with povidone-iodine. Throughout the procedure, strict aseptic techniques were adhered to in order to prevent bacterial contamination. Postoperatively, the mice were allowed to recover in a warm environment before being transferred to isolated cages.

Intramedullary injection of FM1-43FX and FB in mice

Mice were intramedullary injected with 1.25% FB (Polysciences: 17740-1) into the tibial marrow cavity. Three days later, the mice were euthanized, and the ipsilateral L2-3 DRGs were collected for Piezo2 and CGRP immunofluorescence staining and FB fluorescence imaging. FM1–43FX (Invitrogen: 35355) was resuspended in Hanks' Balanced Salt Solution (HBSS, 10 mM HEPES, pH 7.4) at a concentration of 200 μM. Following the establishment of the mouse tibial implant model, the mice were intraperitoneally injected with the FM1–43FX working solution. After 24 hours, the mice were euthanized, and the ipsilateral L2-3 DRGs were collected for fluorescence imaging[31].

OS device implantation model

Mice were anesthetized using a precision vaporizer with 2–3% isoflurane, and the hair on the back was completely removed. Following disinfection with povidone-iodine and draping, a midline skin incision was made along the spine. Blunt dissection was used to separate the muscles to the right transverse process, which was partially removed using a micro drill to expose the DRG. The OS device was carefully implanted subcutaneously and the μ-LED was positioned above the DRG. It was secured to the surrounding muscles to maintain the device's position. The back muscles were repositioned, and the skin incision was closed with sutures. The area was disinfected again with povidone-iodine. Throughout the procedure, strict aseptic techniques were followed to prevent bacterial contamination. Postoperatively, the mice were allowed to recover in a warm environment before being transferred to isolated cages.

Bioinformatics analysis

Bioinformatics analysis was conducted on the bone tissue surrounding the implants to perform transcriptome analysis, aiming to investigate the mechanisms by which OS of mechanoreceptive nerves affects implant osseointegration. To assess the transcriptome of the bone tissue surrounding the implants, total RNA was collected from the peri-implant bone tissue one-week post-surgery, as well as from the BMSCs cultured in vitro for one-week, and subjected to high-throughput sequencing. GO and KEGG analyzes were used to examine the molecular mechanisms and enriched signaling pathways influenced by OS on implant osseointegration. In this study, genes with a log2 fold change (FC) > |1| and a *p*-value < 0.05 were defined as differentially expressed genes (DEGs). Hierarchical clustering heatmap analysis was employed to estimate the overall expression trends of DEGs among different groups. To elucidate the biological significance of the DEGs, enrichment analysis of cellular functional processes and key pathways was performed using the GO and KEGG databases, with a *p*-value < 0.05 as the threshold. Additionally, GSEA was conducted to identify significantly enriched pathways and biological processes in the context of OS, providing a comprehensive understanding of the underlying molecular mechanisms.

qRT-PCR

To evaluate the effects of implants with different elastic moduli on the expression of the IMM FAK and key osteogenic genes (ALP, RUNX2, OPN, and OCN), tibiae and surrounding tissues from two groups of mice were collected between 0 and 21 days post-tibial prosthesis implantation. After dissection, the tibiae and surrounding tissues were washed with PBS, ground in liquid nitrogen, and total RNA was extracted using Trizol reagent (Thermo Fisher). Single-stranded complementary DNA (cDNA) was synthesized using the TransScript® Uni All-in-One First-Strand cDNA Synthesis SuperMix (TransGen Biotech), and qRT-PCR was performed using the PerfectStart® Green qPCR SuperMix (TransGen Biotech) and the StepOnePlus Real-Time System (Applied Biosystems). Each group included at least 3 biological replicates, and all reactions were performed in triplicate. mRNA expression levels were normalized to glyceraldehyde-3-phosphate dehydrogenase (GAPDH). Results are presented as normalized linearized Ct values relative to the reference value $e^{\wedge 2-\Delta\Delta Ct}$. The 5′ and 3′ primers used were as follows: **FAK:** GCGCTGGCTGGAAAAAGAGGAA and TCGGTGGGTG CTGGCTGGGGTAGG; **ALP:** GGACCATTCCCACGTCTTCAC and CCTT GTAGCCAGGCCCATTG; **RUNX2:** CGCCTCACAAACAACCACAG and GGTAGTGACCTGCGGAGATT; **OPN:** CCCGGTGAAAGTGACTGATT and TTCTTCAGAGGACACAGCATTC; **OCN:** TCACACTCCTCGCCCTATTG and GGGTCTCTTCACTACCTCGC; **CGRP:** CTGGCTGCACTGGTGCAG GAC and CGGAAACCGTCCGCGGCGTC **GAPDH:** AAGGCCGGGGCC CACTTGAA and GGACTGTGGTCATGAGCCCTTCCA. GAPDH was used as an internal standard for normalization.

Lithium battery model

The rechargeable lithium battery (10 mAh, 0.15 g) integrated into the Bluetooth device is manufactured through a precise and highly controlled process. The cathode, composed of lithium cobalt oxide ($LiCoO_2$), and the graphite anode are prepared by coating their respective active materials onto aluminum and copper foils, followed by drying and compression. A non-aqueous electrolyte containing a lithium salt ($LiPF_6$) is injected to facilitate ion transport. The electrodes are assembled with a microporous separator within a compact casing, which is then hermetically sealed to ensure stability and prevent leakage. To enhance biocompatibility and safety for in vivo applications, the battery is encapsulated with a biocompatible polymer coating. Each unit undergoes rigorous quality control testing to verify its capacity, voltage consistency, and thermal stability, ensuring reliable performance in biomedical applications.

Fabrication and assembly of the LED and bluetooth main control components

A fully implantable wireless rechargeable OS device was created using etched PCB technology, comprising five layers. Copper traces were patterned on each 100µm-thick glass fiber substrate (Kingboard Holdings Limited). Sixteen turns of 35µm-thick copper wire were etched on the outer edge of the four-layer printed board to form a wireless charging receiving coil with an inductance of ~5µH. Low-temperature solder paste (T5, SMDLTLFP10T5, chip-quik) was used to mount a low-power Bluetooth 5.0 chip (BLE-SoC 5.0, NRF52832, Nordic) and other electronic components on the copper electrodes of the 35µm-thick substrate. These components were soldered in a reflow oven (AS-5060, SMTmax) with a peak temperature of 215 °C and a soldering time of 90 seconds. Similarly, micro-scale light-emitting diode (µ-LED, KPG-0603PBC-TT-5MAV, Kingbright) probes were fabricated on a flexible polyimide (PI) substrate coated with 25µm-thick copper wire. The copper layers measured 130µm high, 300µm wide, and 17.5 µm long. The probes were assembled along their length on a flexible circuit, with µ-LEDs connected to the probe tips. Finally, polydimethylsiloxane (PDMS, 0.6 mm; Sylgard 184; Dow Corning) was injected into an aluminum mold and allowed to solidify, encapsulating the device.

Circuit design and fabrication

The battery charging circuit comprises two main components: a voltage full-wave rectifier circuit with a wireless energy receiving coil and a Schottky diode, and a lithium battery charging management circuit. The receiving coil includes a 5µH inductor and a parallel 110 pF capacitor, resonating at 6.78 MHz. The full-wave rectifier circuit, made up of Schottky diodes, converts AC to DC voltage, which is filtered by a capacitor before reaching the lithium battery charging management circuit. The rectifier circuit consists of four Schottky diodes (model B1040A2, 40 V, 1 A, Jiangsu Changjing) and one capacitor. In a 6.78 MHz alternating magnetic field, the coil and capacitor resonate, coupling electromagnetic energy. The lithium battery provides a stable current for the BLE-SoC 5.0 and µ-LED.

Manufacturing an RF transmitter for wireless energy transfer

The RF transmission system includes a fundamental frequency generator, a Class-E amplification circuit, a transmission loop coil, a cooling fan (model AFB0812 VH, 12V 0.21 A 8 cm, Delta), and a DC power supply. The circular antenna assembly has a resonant frequency matching circuit. The Class-E amplification circuit converts the fundamental frequency into the necessary AC signal, which is sent to the circular coil, creating an alternating magnetic field to transfer energy to the induction coil. Adjusting the matching capacitor of the transmission antenna achieves conjugate matching, maximizing AC current in the circular coil. Optimizing the Class-E amplification circuit's parameters achieves 95% efficiency, allowing it to output 50 W of wireless power at normal temperatures without fan cooling.

Thermal effects of the OS device

The temperature and heat distribution of the OS element directly affect its performance and reliability. Due to the small size of the µ-LED chip, traditional contact temperature measurement methods are impractical. Electrical methods measure the average temperature, not the distribution. An infrared (IR) camera (A655sc, FLIR Systems) records the thermal characteristics and temperature changes of the device. Under typical OS conditions (<40% duty cycle, <50 mW/mm^2), temperature changes were tested at power levels of 40, 80, and 100 mW/mm^2, with duty cycles from 0–60%, over a 15-minute period.

Simulation and Efficiency Analysis

Voltage and current data were measured in a simulation test. The source power (Psource) and load power (Pload) were calculated using $P = V \times I$. The transmission efficiency was derived as: Efficiency = (Pload/Psource) × 100%.

Measurement of mechanical sensitivity thresholds

Mice were housed individually in transparent chambers (7.5 × 7.5 × 15 cm^3) placed on metal mesh. Mechanical hyperalgesia was examined using von Frey filaments and the up–down method. The 50% paw withdrawal threshold (PWT) calculated using the formula: 10[Xf + kδ]/10,000, where Xf is the final von Frey filament value (log units), k is the response pattern, and δ is the mean difference between stimuli (log units)[65].

Measurement of heat sensitivity thresholds

Each mouse was placed on glass platform of the Hargreaves apparatus (Ugo Basile, Italy). A radiant heat source was applied to the plantar surface of the hind paw to measure heat hyperalgesia and the duration before paw withdrawal[66].

Assessment of motor coordination

To evaluate motor coordination, balance, and learning abilities, the rotarod test was conducted. Animals walked on a rotating rod to maintain balance and avoid falling. A 60-second training session at 5 RPM preceded the test. During the experiment, the animals were placed on rods rotating at speeds from 4 to 40 RPM for 300 seconds. Latency to fall, or the time spent on the rod before falling, was measured over three daily trials with 15-minute intervals, and the mean latency was calculated.

Weight-bearing swimming test

The mice were divided into two groups based on the presence of an OS device implant. Following prior studies[67], each mouse was weighed, and a lead block equal to 10% of its body weight was attached to its tail. Mice were placed individually in a 50 × 50 × 40 cm swimming pool, with water at $25 \pm 1\,°C$ and a depth of 30 cm, and a timer was started. If a mouse was submerged for seven seconds without resurfacing, the timer was stopped, and the mouse was promptly removed and dried. A glass rod was gently stirred during the test, and mice swam until exhausted. The swimming duration for each mouse was recorded.

Open field test

The exploratory behavior of mice was evaluated using an open field apparatus (SmartFrame, Kinder Scientific) with a 40 × 40 cm floor and 38 cm high walls. Horizontal movement was detected by infrared sensors placed 2.5 cm apart at a height of 1 cm, while vertical activity (such as rearing) was tracked by a second row of sensors 5 cm above the floor. Mice were placed in the center of the apparatus and observed for 10 minutes. No experimenters were present in the room during the observation period.

CPP test

In the ENV-515S apparatus by Med Associates, the arena is divided into two compartments (each 43 × 21 cm) using acrylic glass dividers to assess mice's real-time spatial preference. During habituation, the dividers are removed, allowing free exploration. In the training phase, mice in the unstimulated compartment receive Non_OS ("off stimulation"), while those in the stimulated compartment receive wireless OS ("stimulation," 10 mA, 10 ms, 2HZ). During testing, mice explore the entire area without stimulation, and their time in each compartment is recorded for 15 minutes. Time spent in each compartment is calculated using Activity Monitor 7 software (Med Associates).

OS Activation of the DRG

To confirm effective OS of nociceptive neurons (Nav1.8) and mechanosensory neurons (Piezo2), we applied synchronized single-pulse OS to Nav1.8$^+$ neurons in Nav1.8::ChR2 mice and Piezo2$^+$ neurons in Piezo2::ChR2 mice. Following stimulation, we conducted mechanical sensitivity, heat sensitivity, and CPP tests. Stimulation parameters were 2 Hz frequency, 10 ms pulse width, applied continuously for 30 minutes, with tests conducted immediately after stimulation. Additionally, to study the effect of OS activation of mechanosensory neurons on neuropeptide secretion, Piezo2::ChR2 mice underwent 30 min (10 mA, 10 ms, 2 Hz) wireless OS twice daily for 7 consecutive days, with littermate controls (*Piezo2-Cre*$^{-/-}$::ChR2$^{+/-}$). We assessed the outcome by harvesting bone tissue surrounding the implants 7 days post-stimulation.

ELISA

To evaluate the biocompatibility of OS components, tail vein blood was collected from mice on the 7th day post-implantation to assess liver function (ALT, AST) and kidney function (Cr, BUN). Briefly, after restraining the mice, the tail was swabbed with an alcohol-soaked cotton ball to dilate the vein. Using a 1 ml syringe and a small flashlight for illumination, ~0.2 ml of blood was drawn from the distal third of the tail vein. The samples were stored in lithium heparin-coated tubes and analyzed using ELISA kits (Elabscience, United States). To study changes in neuropeptide expression around the implants following Piezo2$^+$ neuron stimulation, tibia and surrounding tissues were collected from mice after one week of stimulation (10 mA, 2 Hz, 10 ms, 30 min, twice daily). Measured neuropeptides included CGRP, SP, VIP, and NPY (R&D Systems, Lille, France). To study changes in the expression of inflammatory proteins around the implants following optical stimulation, tibia and surrounding tissues were collected from mice after two weeks of stimulation (10 mA, 2 Hz, 10 ms, 30 min, twice daily) in the Non_OS, OS, and ES groups. Measured inflammatory proteins included IL-1β, IL-6, IL-10, and TGF-β (R&D Systems).

X-ray examination

X-ray imaging of mouse tibiae and OS device was performed at 2 and 4 weeks post-implantation. Mice were placed in a prone position and imaged using an animal X-ray machine (KUBTEC, Parameter) to assess implant stability, loosening, and related complications.

micro-CT analysis

To assess the newly formed bone and bone architecture surrounding the implants, micro-CT imaging was performed using a Skyscan 1172 scanner (Bruker, Kontich, Belgium). The tibial segments with implants were scanned, and a region of interest (ROI) with a thickness of 0.1 mm distal to the implant surface was selected for axial trabecular volume analysis. Post-scanning, 3D images were reconstructed using Skyscan evaluation software, followed by 3D morphometric analysis. The measurements included the percentage of bone volume relative to BV/TV, Tb.Th, Tb.N, Tb.Sp, BMD of BV and the percentage of BIC% as indicators of the quantity and distribution of new bone formation and implant osseointegration.

Histological analysis of bone tissue surrounding the implant

Following micro-CT analysis, bone tissue samples containing implants were decalcified in 12.5% ethylenediaminetetraacetic acid (EDTA) and then embedded in paraffin. Each sample was sectioned into continuous slices of 5 µm thickness using an EXAKT 300 CP microtome (EXAKT Technologies, Germany). The sections were stained with methylene blue-acid fuchsin for general histological evaluation. Similarly, bone tissue sections without implants were stained for ALP and Goldner's Trichrome to assess osteogenic capacity and new bone formation. Histological images were captured under an Olympus Slideview VS200 slide scanner (Olympus, Shinjuku, Japan) and quantitatively analyzed using ImageJ software.

BMSCs isolation

BMSCs were isolated from the femurs of C57BL/6 mice euthanized by isoflurane anesthesia followed by cervical dislocation. Cells were cultured in α-minimum essential medium (α-MEM: 22571; Gibco™, USA) supplemented with 1% penicillin-streptomycin (SV30010; HyClone, USA) and 10% fetal bovine serum (FBS: 10270-106; Gibco™, USA), under conditions of 37 °C and 5% CO2[68]. Cells from the third to fifth passages were used for the studies. Osteogenic differentiation medium (OM) comprised α-MEM enriched with 1% penicillin-streptomycin, 10% FBS, 10 nM dexamethasone, 10 mM β-glycerophosphate, and 173 µM L-ascorbic acid[69].

DRG neurons culture

DRGs were harvested from 8 to14 week-old mice. Procedures were performed under sterile conditions. DRGs were carefully dissected through the intervertebral foramen. The extracted DRGs were transferred to Neurobasal A medium (Thermo Fisher) and finely minced using microscissors. The minced tissues were centrifuged at 1000 rpm for 3 min, and the supernatant was discarded. The minced tissue was digested using containing collagenase A (1.25 mg/mL, Sigma–Aldrich) and dispase II (2.5 mg/mL, Sigma–Aldrich) at 37 °C for 15 minutes. Following digestion, the mixture was centrifuged at 1,000 rpm for 5 minutes at 4 °C, and the supernatant was discarded. The tissue was then resuspended in Neurobasal A medium supplemented with 10% FBS to halt the digestion process, and it was incubated with 150 U/mL DNAse I (TransGen Biotech). To achieve a single-cell suspension of the DRG neurons, mechanical trituration was performed by sequentially aspirating and ejecting the mixture through sterile needles. The resulting cell suspension was filtered through a 70 µm cell strainer and centrifuged again at 1000 rpm for 5 minutes at 4 °C. Finally, the dissociated DRG neurons were resuspended in DRG culture medium, which consisted of Neurobasal A medium supplemented with 50 ng/mL nerve growth factor (NGF, Thermo Fisher) and 10 µM cytosine arabinoside (Sigma), and plated onto plates coated with 10 µg/mL laminin.

OS of DRG neurons

DRGs were isolated from mice expressing Piezo2::ChR2 and digested for culture. The DRG neurons were then divided into two groups: a stimulation group (OS) and a non-stimulation group (Non_OS). The OS group received stimulation parameters of 10 mA, 10 ms, and 2 Hz for 30 minutes. Subsequently, supernatants from both groups were collected.

SEM analysis

To assess the impact of supernatants from OS stimulated DRG neurons expressing Piezo2::ChR2 on the adhesion of BMSCs to implant disks, BMSCs were co-cultured with the implant disks and divided into two groups. One group received supernatant from the OS group, while the other received supernatant from the Non_OS group, both in α-minimum essential medium (α-MEM: 22571; Gibco™, USA). After 7 days of co-culture, the implant disks were removed, washed three times with PBS, fixed in 4% formaldehyde and then in electron microscopy fixative. SEM was performed to evaluate the adhesion of BMSCs on the surface of the implant disks.

ALP staining

To evaluate the effect of supernatants from ChR2-expressing mouse DRG neurons stimulated by light on the osteogenic differentiation of BMSCs, ALP activity assay was initially performed. BMSCs were cultured for 14 days in OM supplemented with supernatants collected from both groups. After culturing for a specified period, cells from different samples were lysed by adding 100 µL of 1% Triton X-100 and incubated in a 37 °C water bath for one hour. Subsequently, ALP activity and total protein content were measured using a commercial ALP activity assay kit (Nanjing Jiancheng Bioengineering Institute, China) and a bicinchoninic acid (BCA) protein assay kit (Solarbio, China), respectively, following the manufacturers' instructions. Relative ALP activity per well was then normalized to the corresponding total protein content. Images were captured using an inverted research microscope (ECLIPSE Ts2R-FL, Nikon, Japan).

Alizarin red staining

BMSCs were cultured for 21 days in OM supplemented with supernatants collected from two groups, followed by staining with Alizarin Red (Sigma, USA) to assess the formation of calcified nodules. After staining, the dye was extracted using 1% cetylpyridinium chloride solution, and the staining intensity was quantitatively measured at 562 nm using a spectrophotometer (BioTek, Germany).

WB analysis

We employed WB analysis to assess the protein expression levels of FAK (Zenbio, R24276, 1:500), p-FAK (Zenbio, 381143, 1:500), RUNX2(ABclonal, A2851,1:2000), ALP (ABclonal, A0514, 1:5000), OPN (ABclonal, A21084, 1:1000), OCN (Zenbio, 614487, 1:500), GAPDH (ABclonal, A19056, 1:10000), HRP goat anti-mouse IgG (H + L) (ABclonal, AS055,1:1000), HRP goat anti-rabbit IgG (H + L) (ABclonal, AS056, 1:100). Proteins were separated by Sodium Dodecyl Sulfate Polyacrylamide Gel Electrophoresis (SDS-PAGE) using equal amounts of protein (20 µg) and then transferred onto polyvinylidene fluoride (PVDF) membranes. The membranes were blocked in 50 g/L non-fat milk in Tris-Buffered Saline with Tween (TBST) for 2 hours, followed by overnight incubation at 4 °C with primary antibodies. Membranes were washed three times with TBST and incubated with secondary antibodies for 1 hour. Protein expression was detected using enhanced chemiluminescence. GAPDH was used as a loading control. Bands were imaged, and band densitometry was quantified using ImageJ software (National Institutes of Health, USA).

BMSCs immunofluorescence staining

After culturing BMSCs in osteogenic medium with different supernatants for 7 days, wash the cells three times with PBS. Fix the cells with 4% paraformaldehyde for 30 minutes and permeabilize with 0.1% Triton X-100 for 20 minutes. Block with 1% bovine serum albumin for 1 hour. Subsequently, incubate the cells with primary antibodies against ALP (Abcam, ab224335, 1:200), RUNX2 (Abcam, ab192256, 1:1000), OPN (Abcam, ab214050, 1:50), and OCN (Proteintech, 23418-1-AP, 1:400) at 4 °C overnight. Then, further incubate the cells with Goat anti-Rabbit IgG Alexa Fluor 488 (Abcam, ab150077, 1: 500) for 30 minutes, followed by nuclear staining with 4',6-diamidino-2-phenylindole (DAPI) for 5 minutes. Observe the immunofluorescently stained cells using a laser scanning confocal microscope (Leica Q500MC, Leica, Germany).

Bone marrow collection

Following humane euthanasia, the femora of the mice were carefully removed and placed on ice. The adjacent muscles were meticulously stripped away, and the distal epiphysis was separated from the femoral shaft. The proximal end of the femur was then excised, and a 25-gauge needle was inserted into the distal portion. A total of 1 ml of cold PBS or α-MEM (Gibco, Thermo Fisher Scientific) was injected by gently depressing the plunger, allowing the bone marrow to be collected into a 1.5 ml centrifuge tube. The harvested bone marrow was subjected to centrifugation at 800 × *g* for 5 minutes at 4 °C for subsequent experiments or cell culture[70].

Tissue immunofluorescence staining

After euthanizing each group of mice ($n = 5$), perfuse the heart with 50 ml of PBS, followed by 50 ml of 4% paraformaldehyde (PFA) for fixation. Dissect the upper segment of the tibia, DRG, and sciatic nerve, and immerse them in 4% PFA for one day. Dehydrate with 30% sucrose, embed in paraffin, and section into 20 µm slices. Treat the sections with PBS containing 1% bovine serum albumin (BSA) and 0.3% Triton at room temperature for 2 hours. Incubate the tissues with primary antibodies, including mouse anti-CGRP (Abcam, ab81887, 1: 100), and rabbit anti-piezo2 (Novus Biologicals, Littleton, CO, 1:500) at 4 °C overnight. After washing off the primary antibodies, incubate with secondary antibodies, including goat anti-mouse IgG Alexa Fluor 488 (Abcam, ab150113, 1: 500), and goat anti-rabbit IgG Alexa Fluor 594 (Abcam, ab150080, 1: 500) at room temperature for 2 hours. FB-labeled samples are not subjected to nuclear staining; the remaining sections are stained with DAPI for nuclei. Acquire fluorescent images using a laser scanning confocal microscope (Leica Q500MC, Leica, Germany). For determining the proportion of CGRP/piezo2-positive neurons in the DRG, calculate the average from L2-3 DRGs, with five randomly selected non-adjacent sections per DRG. Two independent researchers count the CGRP-immunoreactive neurons with visible nuclei and average the results.

Local application of inhibitors/antagonists at the implant site

In the Ti6Al4V+Inject CGRP implant group, CGRP (100 nM, ab47101, Abcam, Cambridge, MA, USA) was dissolved in 100 µL of protein stabilizer, which contained 2% bovine serum albumin, 0.2% polyvinylpyrrolidone, 0.2% sodium chloride, 20% sucrose, and 0.05% sodium azide (all reagents purchased from Sigma-Aldrich, St. Louis, MO, USA). This solution was directly injected into the implant site daily for three weeks post-implantation. In the study of the CGRP-PKA-FAK signaling axis, BIBN4096BS (BIBN, 300 µg/kg body weight, Shanghai Haoyuan Chemexpress, Shanghai, China) was dissolved in saline containing 2% hydrochloric acid; Rp-8-CPT-cAMP (100 µg/kg body weight, Sigma-Aldrich, St. Louis, MO, USA) was dissolved in sterile DMSO; Y15 (100 µg/kg body weight, MedChem Express, MCE, USA) was dissolved in sterile saline;and SP receptor antagonist L-733060 (100 µg/kg body weight, MedChem Express, MCE, USA). These drugs were directly injected into the implant site daily for two weeks post-implantation using a 5 µL Hamilton syringe.

Statistical analysis

Each experiment was assessed based on the mean ± SEM of at least three tests. Statistical significance was evaluated using analysis of variance (ANOVA) and Student's t-test, implemented in GraphPad Prism 9.5.1 software (USA).

Reporting summary

Further information on research design is available in the Nature Portfolio Reporting Summary linked to this article.

Data availability

The RNA-seq data used in this study are available in the Genome Sequence Archive database under accession code CRA023396. The data that support the findings of this study are available within the paper and their Supplementary Information. Source data are provided with this paper.

References

1. Meng, M. et al. 3D printing metal implants in orthopedic surgery: methods, applications and future prospects. *J. Orthop. Translation* **42**, 94–112 (2023).
2. Labek, G., Thaler, M., Janda, W., Agreiter, M. & Stöckl, B. Revision rates after total joint replacement: cumulative results from worldwide joint register datasets. *J. Bone Jt. Surg. Br.* **93**, 293–297 (2011).
3. Pivec, R., Johnson, A. J., Mears, S. C. & Mont, M. A. Hip arthroplasty. *Lancet* **380**, 1768–1777 (2012).
4. Soares dos Santos, M. P. et al. Instrumented hip joint replacements, femoral replacements and femoral fracture stabilizers. *Expert Rev. Med Devices* **11**, 617–635 (2014).
5. Kunčická, L., Kocich, R. & Lowe, T. C. Advances in metals and alloys for joint replacement. *Prog. Mater. Sci.* **88**, 232–280 (2017).
6. Li, Y. et al. New Developments of Ti-based alloys for biomedical applications. *Materials* **7**, 1709–1800 (2014).
7. Arias-González, F. et al. Laser-deposited beta type Ti-42Nb alloy with anisotropic mechanical properties for pioneering biomedical implants with a very low elastic modulus. *Materials* **15**, 7172 (2022).
8. Kaur, M. & Singh, K. Review on titanium and titanium based alloys as biomaterials for orthopaedic applications. *Mater. Sci. Eng. C. Mater. Biol. Appl* **102**, 844–862 (2019).
9. Livshetz, I. et al. Analyzing the burden of revision total knee arthroplasty in the United States between 2009 and 2016. *J. Knee Surg.* **36**, 121–131 (2023).
10. Oladapo, B. I., Zahedi, S. A. & Omigbodun, F. T. A systematic review of polymer composite in biomedical engineering. *Eur. Polym. J.* **154**, 110534 (2021).
11. Bartolomeu, F. et al. Predicting the output dimensions, porosity and elastic modulus of additive manufactured biomaterial structures targeting orthopedic implants. *J. Mech. Behav. Biomed. Mater.* **99**, 104–117 (2019).
12. Chen, Z., Chen, Y., Ding, J. & Yu, L. Blending strategy to modify PEEK-based orthopedic implants. *Compos. Part B: Eng.* **250**, 110427 (2023).
13. Bandyopadhyay, A., Mitra, I., Goodman, S. B., Kumar, M. & Bose, S. Improving biocompatibility for next generation of metallic implants. *Prog. Mater. Sci.* **133**, 101053 (2023).
14. Shih, Y.-R. V., Tseng, K., Lai, H.-Y., Lin, C.-H. & Lee, O. Matrix stiffness regulation of integrin-mediated mechanotransduction during osteogenic differentiation of human mesenchymal stem cells. *J. Bone Miner. Res.* **26**, 730–8 (2011).
15. Wang, L., You, X., Zhang, L., Zhang, C. & Zou, W. Mechanical regulation of bone remodeling. *Bone Res.* **10**, 16 (2022).
16. Brazill, J. M., Beeve, A. T., Craft, C., Ivanusic, J. & Scheller, E. Nerves in bone: evolving concepts in pain and anabolism. *J. Bone Miner. Res.* **34**, 1393–1406 (2019).
17. Basbaum, A. I., Bautista, D. M., Scherrer, G. & Julius, D. Cellular and molecular mechanisms of pain. *Cell* **139**, 267–284 (2009).
18. Zhao, X., Wu, G., Zhang, J., Yu, Z. & Wang, J. Activation of CGRP receptor-mediated signaling promotes tendon-bone healing. *Sci. Adv.* **10**, eadg7380 (2024).
19. Obeidat, A. M. et al. Piezo2 expressing nociceptors mediate mechanical sensitization in experimental osteoarthritis. *Nat. Commun.* **14**, 2479 (2023).
20. Li, Y. et al. Biodegradable magnesium combined with distraction osteogenesis synergistically stimulates bone tissue regeneration via CGRP-FAK-VEGF signaling axis. *BIOMATERIALS* **275**, 120984 (2021).
21. Mi, J. et al. Implantable electrical stimulation at dorsal root ganglions accelerates osteoporotic fracture healing via calcitonin gene-related peptide. *Adv. Sci. (Weinh.)* **9**, e2103005 (2022).
22. Ai, X., MacPhedran, S. E. & Hall, A. K. Depolarization stimulates initial calcitonin gene-related peptide expression by embryonic sensory neurons in vitro. *J. Neurosci.* **18**, 9294–9302 (1998).
23. Chen, W. et al. The roles of optogenetics and technology in neurobiology: a review. *Fronti. Aging Neurosci.* **14**, 867863 (2022).
24. Kim, C. Y. et al. Soft subdermal implant capable of wireless battery charging and programmable controls for applications in optogenetics. *Nat. Commun.* **12**, 535 (2021).
25. Prigge, M., Rösler, A. & Hegemann, P. Fast, repetitive light-activation of CaV3.2 using Channelrhodopsin 2. *Channels* **4**, 241–247 (2010).
26. Staats, K. et al. Intermittent parathyroid hormone increases stability and improves osseointegration of initially unstable implants. *Bone Jt. Res* **11**, 260–269 (2022).
27. Fabry, B., Klemm, A. H., Kienle, S., Schäffer, T. & Goldmann, W. H. Focal adhesion kinase stabilizes the cytoskeleton. *Biophysical J.* **101**, 2131–2138 (2011).
28. Jiang, M. et al. Fluid shear stress and endothelial cells synergistically promote osteogenesis of mesenchymal stem cells via integrin β1-FAK-ERK1/2 pathway. *Turkish J. Biol.* **45**, 683–694 (2021).
29. Nencini, S. & Ivanusic, J. Mechanically sensitive Aδ nociceptors that innervate bone marrow respond to changes in intra-osseous pressure. *J. Physiol.* **595**, 4399–4415 (2017).
30. Lorenz, M. R., Brazill, J. M., Beeve, A. T., Shen, I. & Scheller, E. L. A neuroskeletal atlas: spatial mapping and contextualization of axon

subtypes innervating the long bones of C3H and B6 Mice. *J. Bone Min. Res.* **36**, 1012–1025 (2021).
31. Villarino, N. W. et al. Labeling PIEZO2 activity in the peripheral nervous system. *Neuron* **111**, 2488–2501.e8 (2023).
32. Park, Y.-J. et al. A Triple-Mode Wireless Power-Receiving Unit With 85.5% System Efficiency for A4WP, WPC, and PMA Applications. *IEEE Trans. Power Electron.* **33**, 3141–3156 (2018).
33. Kleinlogel, S. et al. Ultra light-sensitive and fast neuronal activation with the Ca2+-permeable channelrhodopsin CatCh. *Nat. Neurosci.* **14**, 513–518 (2011).
34. Boyden, E. S., Zhang, F., Bamberg, E., Nagel, G. & Deisseroth, K. Millisecond-timescale, genetically targeted optical control of neural activity. *Nat. Neurosci.* **8**, 1263–1268 (2005).
35. Yamada, A., Yamada, A., Ling, J., Furue, H. & Gu, J. G. Effects of inflammation on the properties of Nav1.8-ChR2-positive and Nav1.8-ChR2-negative afferent mechanoreceptors in the hindpaw glabrous skin of mice. *Mol. Pain.* **20**, 17448069241240452 (2024).
36. Yoo, Y., Kwag, J., Kim, K. & Kim, C. Effects of neuropeptides and mechanical loading on bone cell resorption in vitro. *Int. J. Mol. Sci.* **15**, 5874–5883 (2014).
37. Ma, W., Zhang, X., Shi, S.-H. & Zhang, Y. Neuropeptides stimulate human osteoblast activity and promote gap junctional intercellular communication. *Neuropeptides* **47**, 179–186 (2013).
38. Jusek, G., Reim, D., Tsujikawa, K. & Holzmann, B. Deficiency of the CGRP receptor component RAMP1 attenuates immunosuppression during the early phase of septic peritonitis. *Immunobiology* **217**, 761–767 (2012).
39. Eichholz, K. et al. Human bone marrow stem/stromal cell osteogenesis is regulated via mechanically activated osteocyte-derived extracellular vesicles. *Stem Cells Transl. Med.* **9**, 1431–1447 (2020).
40. Gungordu, H. I. et al. Effect of mechanical loading and substrate elasticity on the osteogenic and adipogenic differentiation of mesenchymal stem cells. *J. Tissue Eng. Regenerative Med.* **13**, 2279–2290 (2019).
41. Wang, L. et al. Calcitonin gene-related peptide stimulates stromal cell osteogenic differentiation and inhibits RANKL induced NF-κB activation, osteoclastogenesis and bone resorption. *Bone* **46**, 1369–1379 (2010).
42. Arkless, K., Argunhan, F. & Brain, S. D. CGRP discovery and timeline. *Handb. Exp. Pharm.* **255**, 1–12 (2019).
43. Olesen, J. et al. Calcitonin gene-related peptide receptor antagonist BIBN 4096 BS for the acute treatment of migraine. *N. Engl. J. Med.* **350**, 1104–1110 (2004).
44. Baral, P. et al. Nociceptor sensory neurons suppress neutrophil and γδ T cell responses in bacterial lung infections and lethal pneumonia. *Nat. Med.* **24**, 417–426 (2018).
45. Marie, P. J., Haÿ, E. & Saidak, Z. Integrin and cadherin signaling in bone: role and potential therapeutic targets. *Trends Endocrinol. Metab.* **25**, 567–575 (2014).
46. Valdivia, A., Avalos, A. M. & Leyton, L. Thy-1 (CD90)-regulated cell adhesion and migration of mesenchymal cells: insights into adhesomes, mechanical forces, and signaling pathways. *Front. Cell Dev. Biol.* **11**, 1221306 (2023).
47. Sato, T. et al. A FAK/HDAC5 signaling axis controls osteocyte mechanotransduction. *Nat. Commun.* **11**, 3282 (2020).
48. Sun, R. et al. Nervous system-driven osseointegration. *Int J. Mol. Sci.* **23**, 8893 (2022).
49. Zhang, Y. et al. Implant-derived magnesium induces local neuronal production of CGRP to improve bone-fracture healing in rats. *NATURE MEDICINE* **22**, 1160–1169 (2016).
50. Zheng, N. et al. Magnesium facilitates the healing of atypical femoral fractures: a single-cell transcriptomic study. *Mater. Today* **52**, 43–62 (2022).
51. Wang, S. et al. Surface modification of titanium implants with Mg-containing coatings to promote osseointegration. *Acta Biomater.* **169**, 19–44 (2023).
52. Wang, H. et al. Mussel-Inspired polydopamine coating: a general strategy to enhance osteogenic differentiation and osseointegration for diverse implants. *ACS Appl Mater. Interfaces* **11**, 7615–7625 (2019).
53. Montgomery, K. L. et al. Wirelessly powered, fully internal optogenetics for brain, spinal and peripheral circuits in mice. *Nat. Methods* **12**, 969–974 (2015).
54. Park, S. I. et al. Soft, stretchable, fully implantable miniaturized optoelectronic systems for wireless optogenetics. *Nat. Biotechnol.* **33**, 1280–1286 (2015).
55. Mickle, A. D. et al. A wireless closed-loop system for optogenetic peripheral neuromodulation. *Nature* **565**, 361–365 (2019).
56. Lu, L. et al. Wireless optoelectronic photometers for monitoring neuronal dynamics in the deep brain. *Proc. Natl Acad. Sci. USA* **115**, E1374–E1383 (2018).
57. Kim, T. et al. Injectable, cellular-scale optoelectronics with applications for wireless optogenetics. *Science* **340**, 211–216 (2013).
58. Burton A., et al. Wireless, battery-free subdermally implantable photometry systems for chronic recording of neural dynamics. *Proc. Natl. Acad. Sci. USA.* **117**, 2835–2845 (2020).
59. Michoud, F. et al. Epineural optogenetic activation of nociceptors initiates and amplifies inflammation. *Nat. Biotechnol.* **39**, 179–185 (2021).
60. Cohen, J. A. et al. Cutaneous TRPV1+ neurons trigger protective innate type 17 anticipatory immunity. *Cell* **178**, 919–932.e14 (2019).
61. Wan, Q. et al. Crosstalk between bone and nerves within bone. *Adv. Sci.* **8**, 2003390(2021).
62. Niedermair, T., Schirner, S., Lasheras, M. G., Straub, R. H. & Grässel, S. Absence of α-calcitonin gene-related peptide modulates bone remodeling properties of murine osteoblasts and osteoclasts in an age-dependent way. *Mech. Ageing Dev.* **189**, 111265 (2020).
63. Cheng, Y. et al. Depression promotes prostate cancer invasion and metastasis via a sympathetic-cAMP-FAK signaling pathway. *Oncogene* **37**, 2953–2966 (2018).
64. Wang, Q. et al. Breaking through the basement membrane barrier to improve nanotherapeutic delivery to tumours. *Nat. Nanotechnol.* **19**, 95–105 (2024).
65. Chaplan, S. R., Bach, F. W., Pogrel, J. W., Chung, J. M. & Yaksh, T. L. Quantitative assessment of tactile allodynia in the rat paw. *J. Neurosci. Methods* **53**, 55–63 (1994).
66. Hargreaves, K., Dubner, R., Brown, F., Flores, C. & Joris, J. A new and sensitive method for measuring thermal nociception in cutaneous hyperalgesia. *Pain* **32**, 77–88 (1988).
67. Huang, W.-C. et al. Effect of curcumin supplementation on physiological fatigue and physical performance in mice. *Nutrients* **7**, 905–921 (2015).
68. Yamada, S., Yassin, M. A., Schwarz, T., Hansmann, J. & Mustafa, K. Induction of osteogenic differentiation of bone marrow stromal cells on 3D polyester-based scaffolds solely by subphysiological fluidic stimulation in a laminar flow bioreactor. *J. Tissue Eng.* **12**, 20417314211019375 (2021).
69. Yamada, S. et al. Unique osteogenic profile of bone marrow stem cells stimulated in perfusion bioreactor is Rho-ROCK-mediated contractility dependent. *Bioeng. Transl. Med* **8**, e10509 (2023).
70. Wang, K. et al. PD-1 blockade inhibits osteoclast formation and murine bone cancer pain. *J. Clin. Invest* **130**, 3603–3620 (2020).

Acknowledgements

The authors thank Professor Qiufu Ma (Harvard Medical School, Boston) and Professor Longzhen Cheng (Southern University of Science and Technology, Shenzhen) for offering the mice in this study and Inper company for assisting us in preparing the wireless optogenetic system.

This project was supported (XinYu F.) in part by the China National Natural Science Foundation (82371375), the talent program of Fujian Province, China (2023ZQNZD007, 2023ZQNRCYX-FXY, YYXQN-FXY2022), (to W.M.Z.) by the China National Natural Science Foundation (82272510).

Author contributions

Q.J.W., Y.C., H.Q.D., Y.Q.C., W.M.Z., and X.Y.F. designed the experiments. Q.J.W., Y.C., H.Q.D., Y.Q.C., X.H.Y., J.H.Lv, J.G.H., J.X.H., C.F.Z., Z.H.H., H.Y.L., Y.H., J.M.L., L.Y., and B.Y. performed the data analysis and created the figures. L.L., S.L.Y., C.H.Z., J.H.Lin, and X.Y.F. contributed to project administration. W.B.L., C.C., B.Y., X.H.Y., and X.Y.F. were involved in data collection. Q.J.W., Y.C., H.Q.D., and Y.Q.C. conducted the in vitro and in vivo experiments and participated in the writing of the manuscript. Q.J.W., Y.C., B.Y., W.M.Z., and X.Y.F. contributed to revising the manuscript. All authors read and approved the manuscript.

Competing interests

The authors declare no competing interests.

Additional information

Supplementary information The online version contains supplementary material available at https://doi.org/10.1038/s41467-025-58336-x.

Correspondence and requests for materials should be addressed to Bin Yang, Wenming Zhang or Xinyu Fang.

Peer review information *Nature Communications* thanks the anonymous reviewers for their contribution to the peer review of this work. A peer review file is available.

Reprints and permissions information is available at http://www.nature.com/reprints